AIAA JOURNAL
Vol. 54, No. 3, March 2016

Detailed Modeling of Plasmas for Computational Aerodynamics

Bernard Parent*
Pusan National University, Busan 609-735, Republic of Korea
Mikhail N. Shneider†
Princeton University, Princeton, New Jersey 08544-5263
and
Sergey O. Macheret‡
Purdue University, West Lafayette, Indiana 4706

DOI: 10.2514/1.J054624

As demonstrated by Parent, B., et al., ("Electron and Ion Transport Equations in Computational Weakly-Ionized Plasmadynamics," *Journal of Computational Physics*, Vol. 259, 2014, pp. 51–69), the computational efficiency of the drift-diffusion plasma model can be increased significantly by recasting the equations such that the potential is obtained from Ohm's law rather than Gauss's law and by adding source terms to the ion transport equations to ensure that Gauss's law is satisfied. Not only did doing so reduce the stiffness of the system, leading to faster convergence, but it also resulted in a higher resolution of the converged solution. The combined gains in convergence acceleration and resolution amounted to a hundredfold increase in computational efficiency when simulating nonneutral plasmas with significant quasi-neutral regions. In this paper, it is shown that such a recast of the drift-diffusion model has yet another advantage: its lack of stiffness permits the electron and ion transport equations to be integrated in coupled form along with the Favre-averaged Navier–Stokes equations. Test cases relevant to plasma aerodynamics (including nonneutral sheaths, magnetic field effects, and negative ions) demonstrate that the proposed coupled system of equations can be converged in essentially the same number of iterations as that describing nonionized flows while not sacrificing the generality of the drift-diffusion model.

Nomenclature

a = speed of sound of neutrals, m/s
$\boldsymbol{B}$ = magnetic field vector, T
C_k = particule charge of kth species, C
c_p = neutrals specific heat at constant pressure, $\partial h_n/\partial T$, J kg^{-1} K^{-1}
CFL = user-defined constant needed to find pseudotime step
D = matrix including extra convection terms associated with charged species
$\boldsymbol{E}$ = electric field vector, $-\nabla\phi$, V/m
E_{div} = user-specified constant related to discretization of electron temperature gradients and typically set to 10 V/m
$\boldsymbol{E}^k$ = the electric field in kth species reference frame, $\boldsymbol{E} + \boldsymbol{V}^k \times \boldsymbol{B}$, V/m
$E^\star$ = reduced electric field in electron reference frame, $|\boldsymbol{E} + \boldsymbol{V}^e \times \boldsymbol{B}|/N$, Vm^2
e = elementary charge, C
e_k = specific energy of kth species, $h_k - P_k/\rho_k$, J/kg
$e_t^\star$ = total energy, $w_{N_2} e_v + \sum_{k=1}^{n_s} w_k e_k + \frac{1}{2}|\boldsymbol{V}^n|^2 + k$, J/kg
e_v = nitrogen vibrational energy, $R_{N_2}\Theta_v/(\exp(\Theta_v/T_v) - 1)$, J/kg
e_v^0 = nitrogen vibrational energy at equilibrium, $R_{N_2}\Theta_v/(\exp(\Theta_v/T) - 1)$, J/kg
$\boldsymbol{F}$ = convection flux vector
$\boldsymbol{G}$ = vector of diffusion variables
$\boldsymbol{H}$ = vector including extra convection terms needed for charged species
h_k = specific enthalpy of kth species at its temperature T_k excluding nitrogen vibrational energy but including heat of formation, obtained using McBride temperature-dependent polynomials, J/kg
h_n = specific enthalpy of neutrals at the temperature T excluding nitrogen vibrational energy but including heat of formation, J/kg
$\boldsymbol{J}$ = current density vector, A/m^2
K = diffusion matrix
k = turbulence kinetic energy, J/kg
k_B = Boltzmann constant, J/K
L_c = user-specified characteristic length scale used to determine pseudotime step of potential equation, m
m_k = particule mass of kth species, kg
N = total number density of mixture, $\sum_k N_k$, m^{-3}
N_k = species number density, m^{-3}
n_{cs} = number of charged species
n_d = number of dimensions
n_s = number of species (including charged species)
P_k = species partial pressure, $\rho_k R_k T_k$, Pa
Pr = adjusted Prandtl number, $\frac{\eta}{\kappa}\left(c_p + w_{N_2}\frac{\partial e_v^0}{\partial T}\right)$
Pr_t = turbulent Prandtl number, typically set to 0.9
$P^\star$ = effective pressure including turbulence and electron energy contributions, $\frac{2}{3}\rho k + \sum_{k=1}^{n_s} P_k$, Pa
Q_b = electron beam power deposited, W/m^3
$Q_b^\star$ = reduced electron beam power deposited, Q_b/N, W
Q_k = turbulence kinetic energy production term, W/m^3
Q_J^e = electron Joule heating, $\frac{1}{\mu_e}|C_e|N_e|\boldsymbol{V}^e - \boldsymbol{V}^n|^2$, W/m^3
R_k = gas constant of kth species, J/kgK
$\boldsymbol{R}_\Delta$ = discretized residual vector
$\boldsymbol{S}$ = source term vector
Sc_t = turbulent Schmidt number, typically set to 1
s_k = sign of charge of species k (either $+1$ for positive species or -1 for negative species)
T = neutrals and ions temperature, K
T_e = electron temperature, K
T_k = temperature of kth species, K

Presented as Paper 2015-3104 at the 45th AIAA Thermophysics Conference, Dallas, TX, 22–26 June 2015; received 21 July 2015; revision received 7 October 2015; accepted for publication 8 October 2015; published online 6 January 2016.

*Associate Professor, Department of Aerospace Engineering; bernparent@gmail.com.
†Senior Research Scientist, Department of Mechanical and Aerospace Engineering.
‡Professor, School of Aeronautics and Astronautics.

T_v = nitrogen vibrational temperature, K
t = time, s
$\boldsymbol{U}$ = vector of conserved variables
$\boldsymbol{V}^n$ = velocity of neutrals, m/s
$\boldsymbol{V}^r$ = rth species velocity, m/s
W_k = mass production of species k per unit volume due to chemical reactions, kg/s
w_k = mass fraction of kth species, ρ_k/ρ
X_i = grid index along ith dimension
$X_{i,j}$ = $\partial X_i/\partial x_j$, 1/m
x, y, z = Cartesian coordinates, m
x_i = Cartesian coordinates, m
$\boldsymbol{Y}$ = vector function of electric field and current density
Z = matrix related to unsteady terms
z = row number of N_2 mass conservation equation
α = nondimensional mass-based ambipolar tensor
β_k^c = 1 if species k is charged species, zero otherwise
β_k^e = 1 if species k is electron, zero otherwise
β_k^n = 1 if species k is a neutral, zero otherwise
β_k^+ = 1 if species k is positive ion, zero otherwise
β_k^- = 1 if species k is negative ion or electron, zero otherwise
Γ = preconditioning matrix, 1/s
γ = secondary emission coefficient
$\boldsymbol{\Delta V}^r$ = velocity contribution due to magnetic field for rth species, m/s
Δx_i = grid spacing along ith dimension, m
$\Delta\tau$ = pseudotime step used to integrate coupled drift-diffusion Navier–Stokes system, s
$\Delta\tau_\phi$ = pseudotime step used to integrate potential equation, s
$\Delta^n(\cdot)$ = pseudotime difference operator, $(\cdot)^{n+1} - (\cdot)^n$
δ_{rk} = Kronecker delta
$\delta_{x_i}(\cdot)$ = discretization of derivative $\partial(\cdot)/\partial x_i$
ϵ_0 = permittivity of free space, $\mathrm{m^{-3}\ kg^{-1}\ s^4\ A^2}$
ζ_D = user-specified parameter related to eigenvalue conditioning of $D^\pm$ matrices and typically set to 0.2
ζ_v = fraction of electron Joule heating that is consumed in excitation of vibration levels of nitrogen molecule
ζ_Γ^e = user-specified parameter related to preconditioning of electron transport equation and typically set to 0.001
ζ_Γ^i = user-specified parameter related to preconditioning of ion transport equations and typically set to 0.1
η = viscosity of neutrals mixture, obtained from Wilke's mixing rule, Pa s
$\eta_k^\star$ = k transport equation diffusion coefficient, $\eta + 0.5\eta_t$, Pa s
η_t = turbulence viscosity, $0.09\rho k/\omega$, Pa s
$\eta_\omega^\star$ = ω transport equation diffusion coefficient, $\eta + 0.5\eta_t$, Pa s
$\eta^\star$ = effective viscosity including turbulence contribution, $\eta + \eta_t$, Pa s
Θ_v = nitrogen characteristic vibration temperature, 3353 K
κ = thermal conductivity of neutrals mixture obtained from Mason and Saxena relation, W/(m K)
κ_e = electron thermal conductivity, $(5/2)k_\mathrm{B}^2 N_e \mu_e T_e/|C_e|$, W/(m K)
κ_v = nitrogen vibrational thermal conductivity, $w_{N_2}\frac{\eta}{Pr}\frac{\partial e_v}{\partial T_v}$, W/(m K)
$\kappa_v^\star$ = effective nitrogen vibrational thermal conductivity including turbulence contribution, $w_{N_2}\left(\frac{\eta}{Pr} + \frac{\eta_t}{Pr_t}\right)\frac{\partial e_v}{\partial T_v}$, W/(m K)
$\kappa^\star$ = effective thermal conductivity including turbulence contribution, $c_p\left(\frac{\eta}{Pr} + \frac{\eta_t}{Pr_t}\right)$, W/(m K)
μ_k = mobility of kth species, $\mathrm{m^2/(V\ s)}$
$\tilde{\mu}^k$ = tensor mobility of kth species, $\mathrm{m^2/(V\ s)}$
ν_k = mass diffusion coefficient for neutral species, determined from Wilke's rule, kg/(m s)
$\nu_k^\star$ = effective mass diffusion coefficient for neutral species including turbulence contribution, $\nu_k + \frac{\eta_t}{Sc_t}$, kg/(m s)
ρ = density of mixture, $\sum_k \rho_k$, $\mathrm{kg/m^3}$
ρ_c = net charge density, $\sum_k C_k N_k$, $\mathrm{C/m^3}$
ρ_e = electron partial mass density, $\mathrm{kg/m^3}$
ρ_k = partial mass density of kth species, $\mathrm{kg/m^3}$
σ = conductivity, $\sum_k |C_k| N_k \mu_k$, S/m
σ_ref = user-specified reference conductivity used to determine pseudotime step of potential equation, S/m
τ_{vt} = nitrogen vibration-translation relaxation time, s
ϕ = electric field potential, V
χ = coordinate perpendicular to surface and pointing toward fluid, m
ψ = nondimensional tensor related to Navier–Stokes stresses
Ω = inverse of metrics Jacobian
ω = specific dissipation rate of turbulence kinetic energy, 1/s

Superscripts

n = pseudotime level
$\star$ = generalized coordinates

I. Introduction

PLASMA aerodynamics, or plasma flow control, has in recent years been demonstrated through various experiments to be potentially capable of improving significantly the performance of aircraft either through dielectric barrier discharge (DBD) actuators or through magnetohydrodynamic (MHD) generators and accelerators. Experiments have indeed shown DBD and MHD devices to be viable in preventing separation on the leading edge of subsonic airfoils [1,2], in reducing losses in turbojet compressors [3], in reducing aircraft noise [4,5], in controlling boundary-layer transition [6–8], in reducing turbulent boundary-layer thickness [9], in enhancing jet mixing [10], in controlling shock–boundary-layer interaction [11], or in generating power aboard hypersonic flight vehicles [12].

However, there are various physical phenomena encountered in plasma flow control experiments that are incompletely understood due to the difficulty in simulating numerically such experiments. Indeed, numerical simulations of plasma aerodynamics have been limited so far either to 1) strictly plasma simulations, in which the electron and ion transport equations are solved (through fluid or kinetic models) while neglecting their impact on the neutrals [13–20]; 2) strictly Navier–Stokes simulations, in which the Navier–Stokes equations with approximate plasma source terms to account for the Coulomb/Lorentz forces are solved independently of the charged species [21–27]; 3) MHD simulations, in which the Euler or Navier–Stokes equations augmented with Lorentz forces are solved in conjunction with plasma equations in the quasi-neutral state [28–31]; or more rarely 4) loosely coupled simulations, in which the charged species and the Navier–Stokes equations are integrated using two different modules with greatly varying integration step lengths [32,15]. The first three approaches suffer from an incomplete physical model that either neglects the dependence of the charged species on the neutrals (or vice versa) or assumes that the plasma is in the quasi-neutral state. Although the fourth approach, the loosely coupled strategy, provides a more accurate physical model, it is seldom the method of choice because it leads to excessive grid-induced error (due to the too-low integration step length of the charged species leading to a too-large number of iterations and hence preventing the use of fine-enough grids).

The integration in coupled form of both the charged species and the Navier–Stokes equations without assuming quasi neutrality and using an integration step length similar to the one used in nonionized aerodynamics would be advantaged over all previous strategies by keeping both the physical error and the grid-induced error low, hence leading to a significant enhancement in the quality of numerical results for plasma aerodynamics. Unfortunately, this has proven not to be feasible so far due to the high stiffness associated with the electron and ion transport equations in which the velocity is determined from the drift-diffusion model and the electric field is determined from Gauss's law. The stiffness of such a system of equations was commonly attributed to the large discrepancy of the physical time scales involved.

Indeed, such a set of equations does offer a large variation of time scales: whereas electrons travel at millions of meters per second within cathode sheaths, the ions travel at a speed less than a few hundred meters per second within quasi-neutral regions. (The large difference in speeds throughout the plasma system is due to the drift velocity of charged species being the product of electric field strength and mobility, with the mobility of electrons exceeding the one of ions by two orders of magnitude and with the electric field strength within the cathode sheath exceeding the electric field strength within the quasi-neutral plasma also by two orders of magnitude.) Because the stiffness could not be overcome through the use of block-implicit methods (which are a well-established strategy to integrate efficiently systems with excessively low time scales originating from chemical reactions or viscous effects), simulations of the drift-diffusion model typically required excessively small integration step lengths leading to millions of iterations to reach convergence. Thus, should the stiff drift-diffusion-based charged species transport equations be integrated in coupled form with the Navier–Stokes equations, the integration step length of the overall system would need to be orders of magnitude lower than the one commonly used to integrate aerodynamic flows, hence requiring excessive computing resources to tackle even the simplest problems.

Recent advances in computational plasmadynamics may enable this hurdle to be surmounted. In [33], it was argued that the stiffness of the drift-diffusion model was not due to the disparate physical time scales but rather due to the potential equation based on Gauss's law amplifying the numerical error associated with the densities within quasi-neutral regions. Indeed, when using a block-implicit method to advance the solution in pseudotime and when linearizing the diffusion, convection, and source terms, it was observed that the drift-diffusion model became stiff only when a quasi-neutral region of substantial size would form within the domain. On the other hand, the drift-diffusion model did not exhibit stiffness when the plasma was free of quasi-neutral regions. Because the physical time scales were essentially the same whether or not the plasma included regions of quasi neutrality, the stiffness associated with the drift-diffusion model could not originate from the discrepancy between the physical time scales. Rather, it was found that the observed stiffness in regions of quasi neutrality originated from Gauss's law amplifying the errors associated with the electron and ion densities (see Sec. 8 in [33] for more details on this point).

To get rid of the stiffness associated with the solution of Gauss's law, a strategy was thus proposed in [33] in which the potential equation is obtained from a form of Ohm's law and some source terms are added to the ion transport equation to ensure that Gauss's law remains satisfied in regions of nonneutrality. As well, it was found beneficial to rewrite the electron transport equation in ambipolar form, following the approach outlined in [34] (but with modifications for a nonneutral plasma) in order to obtain a higher resolution of the converged solution. In doing so, the system of equations was found to be free of stiffness when solved with block-implicit methods and could be converged in 100–1000 times fewer iterations than the standard approach. The newly recast computationally efficient drift-diffusion model was then extended to multicomponent multidimensional plasmas in [35] and to multicomponent plasmas in a magnetic field in [36]. Again, it was found through several test cases that the new approach was considerably more computationally efficient: not only did it require fewer iterations to reach convergence, but it also exhibited a higher resolution of the converged solution. The combined gains in convergence acceleration and in resolution resulted in a 100-fold gain in computational efficiency when compared to the standard drift-diffusion model.

It is emphasized that the computationally efficient Ohm-based governing equations (in which the potential is obtained from Ohm's law) are obtained from the same physical model as the standard Gauss-based governing equations (in which the potential is obtained from Gauss's law) without introducing additional assumptions or simplifications. Because of this, both sets of equations yield the same solution when the grid is refined sufficiently. This was confirmed in [35] and [36], in which several grid convergence studies of nonneutral cathode sheaths, glow discharges, dark discharges, and plasmas contained between dielectrics showed that the Ohm-based system of equations yields the same exact solution as the standard Gauss-based system while being considerable more computationally efficient due to its lack of stiffness and its higher resolution of the converged solution.

In this paper, we show that the computationally efficient Ohm-based drift-diffusion model proposed by the authors in previous papers has yet another advantage: it can be integrated in coupled form with the Navier–Stokes equations. This is in contrast to previous numerical simulations of plasma aerodynamics in which the charged species equations and the neutrals transport equations were solved using two different integration processes (which was necessary due to the conventional drift-diffusion model being too stiff to be integrated in coupled form with the neutrals). Using two different integration strategies not only increases the computational time but can also lead to problems in maintaining monotonicity or conservation of the fluxes when linking the two sets of equations together. Such issues are avoided here by solving all transport equations conjunctly. As will be shown through several test cases of cathode and anode sheaths interacting with turbulent boundary layers, the coupled drift-diffusion and Navier–Stokes system of equations proposed here is remarkably computationally efficient. Indeed, for many problems, a converged solution can be obtained in a couple of thousand iterations, which is essentially the same number of iterations as when simulating nonionized aerodynamic flows.

II. Computationally Efficient Drift-Diffusion Model

As was shown in [33] and later extended to a multicomponent plasma in [35] and to a plasma in a magnetic field in [36], the computational efficiency of the drift-diffusion model can be improved 100-fold or more when recast such that the potential is obtained from a form of Ohm's law rather than Gauss's law. Of course, for such a recast not to alter the physical model, it is necessary to make changes to the ion and electron transport equations to ensure that Gauss's law is satisfied in nonneutral regions. A form of the ion and electron transport equations that satisfies the drift-diffusion model while solved alongside a potential equation based on Ohm's law was determined to be [36]

$$\begin{aligned}
&\sum_{r=1}^{n_s} \alpha_{kr} \frac{\partial \rho_r}{\partial t} + \sum_{i=1}^{3} \sum_{r=1}^{n_s} \frac{\partial}{\partial x_i} \alpha_{kr} (\Delta \boldsymbol{V}_i^r + \boldsymbol{V}_i^n) \rho_r \\
&\quad + \sum_{i=1}^{3} (\beta_k^+ \boldsymbol{E}_i - \beta_k^- \boldsymbol{J}_i) \frac{\partial}{\partial x_i} \mu_k \rho_k \left(\beta_k^+ + \frac{1}{\sigma} \beta_k^- \right) \\
&\quad - \sum_{i=1}^{3} \sum_{r=1}^{n_s} \frac{\partial}{\partial x_i} \left(\frac{\mu_r k_B T_r \alpha_{kr}}{|C_r|} \frac{\partial \rho_r}{\partial x_i} \right) \\
&\quad = W_k - \beta_k^+ \mu_k \rho_k \frac{\rho_c}{\epsilon_0} + \sum_{r=1}^{n_s} \sum_{i=1}^{3} \frac{\partial}{\partial x_i} \left(\frac{\mu_r k_B \rho_r \alpha_{kr}}{|C_r|} \frac{\partial T_r}{\partial x_i} \right)
\end{aligned} \tag{1}$$

where C_k is the charge of species k (equal to e for the singly charged positive ions, to $-e$ for the electrons, to $-2e$ for the doubly charged negative ions, etc.) and ρ_c is the net charge density defined as

$$\rho_c \equiv \sum_{r=1}^{n_s} C_r N_r \tag{2}$$

In addition, $\boldsymbol{J}$ is the current density defined as

$$\boldsymbol{J} \equiv \sum_{r=1}^{n_s} C_r N_r \boldsymbol{V}^r \tag{3}$$

with $\boldsymbol{V}^r$ the species velocity including drift and diffusion, which, for a weakly ionized plasma in a magnetic field, can be shown to correspond to

$$\boldsymbol{V}_i^k = \boldsymbol{V}_i^n + \sum_{j=1}^{3} s_k \tilde{\mu}_{ij}^k \boldsymbol{E}_j^n - \sum_{j=1}^{3} \frac{\tilde{\mu}_{ij}^k}{|C_k| N_k} \frac{\partial P_k}{\partial x_j} \tag{4}$$

with the tensor mobility equal to

$$\tilde{\mu}^k = \frac{\mu_k}{1+\mu_k^2|\boldsymbol{B}|^2}\begin{bmatrix} 1+\mu_k^2\boldsymbol{B}_1^2 & \mu_k^2\boldsymbol{B}_1\boldsymbol{B}_2+s_k\mu_k\boldsymbol{B}_3 & \mu_k^2\boldsymbol{B}_1\boldsymbol{B}_3-s_k\mu_k\boldsymbol{B}_2 \\ \mu_k^2\boldsymbol{B}_1\boldsymbol{B}_2-s_k\mu_k\boldsymbol{B}_3 & 1+\mu_k^2\boldsymbol{B}_2^2 & \mu_k^2\boldsymbol{B}_2\boldsymbol{B}_3+s_k\mu_k\boldsymbol{B}_1 \\ \mu_k^2\boldsymbol{B}_1\boldsymbol{B}_3+s_k\mu_k\boldsymbol{B}_2 & \mu_k^2\boldsymbol{B}_2\boldsymbol{B}_3-s_k\mu_k\boldsymbol{B}_1 & 1+\mu_k^2\boldsymbol{B}_3^2 \end{bmatrix} \tag{5}$$

Further, the nondimensional mass-based ambipolar tensor α is defined as

$$\alpha_{kr} \equiv \frac{m_k}{m_r}\left(\frac{\delta_{rk}\sigma + \beta_k^- C_r \mu_k N_k}{\sigma}\right) \tag{6}$$

and the difference between the velocity of the kth species and the velocity of the kth species should the magnetic field be zero, $\boldsymbol{\Delta V}_i^k$, can be shown to correspond to

$$\boldsymbol{\Delta V}_i^k = \sum_{j=1}^{3} s_k \tilde{\mu}_{ij}^k \boldsymbol{E}_j^n + \sum_{j=1}^{3}\left(\frac{\delta_{ij}\mu_k - \tilde{\mu}_{ij}^k}{|C_k|N_k}\right)\frac{\partial P_k}{\partial x_j} - s_k\mu_k\boldsymbol{E}_i \tag{7}$$

where $\boldsymbol{E}^k$ is the electric field in the kth species reference frame, which stands for

$$\boldsymbol{E}^k \equiv \boldsymbol{E} + \boldsymbol{V}^k \times \boldsymbol{B} \tag{8}$$

In the latter, the electric field $\boldsymbol{E}$ is determined from a form of the generalized Ohm's law applicable to a multispecies mixture [37]:

$$\begin{aligned} &\frac{\partial \rho_c}{\partial t} - \sum_{i=1}^{3}\frac{\partial}{\partial x_i}\left(\sigma\frac{\partial \phi}{\partial x_i}\right) + \sum_{k=1}^{n_{cs}}\sum_{i=1}^{3}\frac{\partial}{\partial x_i}C_k N_k(\Delta \boldsymbol{V}_i^k + \boldsymbol{V}_i^n) \\ &\quad - \sum_{k=1}^{n_{cs}}\sum_{i=1}^{3}\frac{\partial}{\partial x_i}\left(s_k\mu_k N_k k_B\frac{\partial T_k}{\partial x_i}\right) \\ &\quad - \sum_{k=1}^{n_{cs}}\sum_{i=1}^{3}\frac{\partial}{\partial x_i}\left(s_k\mu_k T_k k_B\frac{\partial N_k}{\partial x_i}\right) = 0 \end{aligned} \tag{9}$$

It is emphasized that the Ohm's-law-based system of equations outlined in this section is obtained from the same physical model as the conventional Gauss's-law-based drift-diffusion model and as such has the same exact solution (when the mesh size tends toward infinity). Nonetheless, despite yielding the same solution on refined meshes, the recast drift-diffusion model summarized previously is free of stiffness (when used in conjunction with a block-implicit integration strategy) and is typically 100 times or more computationally efficient for problems characteristic of plasma aerodynamics.

III. Coupled Drift-Diffusion and Navier–Stokes System

Because the new computationally efficient drift-diffusion model outlined in the previous section does not restrict the integration step length to excessively small values, it can be solved in coupled form with the neutrals transport equations through the same integration strategy using aerodynamic-scale time steps. Thus, we regroup here the electron and ion mass conservation equation outlined in Eq. (1) with the conservation equations of the mass, momentum, total energy, vibrational energy, and turbulence kinetic energy and specific dissipation rate that are commonly used in turbulent chemically reacting compressible flow codes. We choose here to close the turbulence transport equations with the Wilcox $k\omega$ model [38] because, in contrast to the $k\epsilon$ models, it can be conveniently integrated through the laminar sublayer of the turbulent boundary layer without the need of wall functions. Using wall functions here would be problematic because it would require the near-boundary node to be located at a too-high distance from the wall, hence preventing enough grid points from being located within the cathode and anode sheaths.

In matrix form, the coupled drift-diffusion and Navier–Stokes system thus becomes

$$\begin{aligned} Z\frac{\partial \boldsymbol{U}}{\partial t} + \sum_{i=1}^{3}\frac{\partial}{\partial x_i}D_i\boldsymbol{U} + \sum_{i=1}^{3}\frac{\partial \boldsymbol{F}_i}{\partial x_i} - \sum_{i=1}^{3}\sum_{j=1}^{3}\frac{\partial}{\partial x_j}\left(K_{ij}\frac{\partial \boldsymbol{G}}{\partial x_i}\right) \\ + \sum_{i=1}^{3}\boldsymbol{Y}_i\frac{\partial \boldsymbol{H}}{\partial x_i} = \boldsymbol{S} \end{aligned} \tag{10}$$

where the vector of conserved variables $\boldsymbol{U}$ and the vector of diffusion variables $\boldsymbol{G}$ correspond to

$$\boldsymbol{U} = \begin{bmatrix} \rho_1 \\ \vdots \\ \rho_{n_s} \\ \rho\boldsymbol{V}_1^n \\ \vdots \\ \rho\boldsymbol{V}_3^n \\ \rho e_t^\star \\ \rho k \\ \rho\omega \\ \rho_{\mathrm{N}_2} e_v \end{bmatrix} \qquad \boldsymbol{G} = \begin{bmatrix} \rho_1\beta_1^c + w_1\beta_1^n \\ \vdots \\ \rho_{n_s}\beta_{n_s}^c + w_{n_s}\beta_{n_s}^n \\ \boldsymbol{V}_1^n \\ \vdots \\ \boldsymbol{V}_3^n \\ T \\ k \\ \omega \\ T_v \end{bmatrix} \tag{11}$$

where the total specific energy $e_t^\star$ includes the sum of the species specific internal energies, the kinetic energy of the neutrals, and the turbulence kinetic energy,

$$e_t^\star = w_{\mathrm{N}_2}e_v + \sum_{k=1}^{n_s} w_k e_k + \frac{1}{2}|\boldsymbol{V}^n|^2 + k \tag{12}$$

with the species specific internal energy obtained from its respective specific enthalpy as $e_k = h_k - P_k/\rho_k$. The species specific enthalpy h_k includes the heat of formation and is found from the species temperature (T_e for the electrons and T for the ions and the neutrals) using polynomials from McBride [44]. Such polynomials are typically valid for most species in the range 200–20,000 K. Should the temperature exceed the limit for which the polynomials are valid, the species enthalpy is assumed calorically perfect in the range exceeding the maximum temperature (either 6000 or 20,000 K depending on the species). Because the nitrogen vibrational energy is taken into account through the nitrogen vibration energy in nonequilibrium, e_v, the specific energy and enthalpy of nitrogen (i.e., e_{N_2} and h_{N_2}) do not include the nitrogen vibrational energy.

It is pointed out that the total energy equation outlined here was obtained by summing the energy equations for the ions, the electrons, and the neutrals. The energy equation for each species was itself obtained from the first law of thermodynamics and the momentum equation (either drift diffusion or Navier–Stokes) applicable to each species. For this reason, the total energy $e_t^\star$ does not include the kinetic energy of the electrons or the ions because the kinetic energy terms originate from the inertia terms within the momentum equations, and the charged species momentum equations based on the drift-diffusion model do not include the inertia terms. Thus, including the kinetic energy of the charged species within the total energy would not be more accurate here because it would lead to a total energy equation that would not satisfy the first law for each charged species.

A third vector needed within the coupled governing equations is the convective flux $\boldsymbol{F}_i$, which corresponds to

$$\boldsymbol{F}_i = \begin{bmatrix} \rho_1\boldsymbol{V}_i^n \\ \vdots \\ \rho_{n_s}\boldsymbol{V}_i^n \\ \rho\boldsymbol{V}_i^n\boldsymbol{V}_1^n + \delta_{i1}P^\star \\ \vdots \\ \rho\boldsymbol{V}_i^n\boldsymbol{V}_3^n + \delta_{i3}P^\star \\ \rho\boldsymbol{V}_i^n e_t^\star + \boldsymbol{V}_i^n P^\star \\ \rho\boldsymbol{V}_i^n k \\ \rho\boldsymbol{V}_i^n\omega \\ \rho_{\mathrm{N}_2}\boldsymbol{V}_i^n e_v \end{bmatrix} \tag{13}$$

where the effective pressure $P^\star$ includes contributions from the neutrals, ions, and electrons (as obtained from Dalton's law) but also from the turbulence kinetic energy,

$$P^\star = \sum_{k=1}^{n_s} P_k + \frac{2}{3}\rho k \tag{14}$$

where the partial pressures are obtained using the ideal gas law $P_k = \rho_k R_k T_k$ with the temperature of the ions and neutrals set to the bulk gas temperature T and the temperature of the electrons determined as a function of the effective electric field (more on this in the following).

Another vector that is needed within Eq. (10) is the source term $\boldsymbol{S}$

$$\boldsymbol{S} = \begin{bmatrix} W_1 - \beta_1^+ \mu_1 \rho_1 \frac{\rho_c}{\epsilon_0} + \sum_{i=1}^3 \frac{\partial}{\partial x_i} \frac{\mu_e k_B \rho_e \alpha_{1e}}{|C_e|} \frac{\partial T_e}{\partial x_i} \\ \vdots \\ W_{n_s} - \beta_{n_s}^+ \mu_{n_s} \rho_{n_s} \frac{\rho_c}{\epsilon_0} + \sum_{i=1}^3 \frac{\partial}{\partial x_i} \frac{\mu_e k_B \rho_e \alpha_{n_s e}}{|C_e|} \frac{\partial T_e}{\partial x_i} \\ \rho_c \boldsymbol{E}_1 + (\boldsymbol{J} \times \boldsymbol{B})_1 \\ \vdots \\ \rho_c \boldsymbol{E}_3 + (\boldsymbol{J} \times \boldsymbol{B})_3 \\ \boldsymbol{E} \cdot \boldsymbol{J} + Q_b + \sum_{i=1}^3 \frac{\partial}{\partial x_i} \kappa_e \frac{\partial T_e}{\partial x_i} \\ Q_k - \rho k \omega \\ \frac{\omega}{k}\left(\frac{5}{9} Q_k - \frac{5}{6}\rho k \omega\right) \\ W_{\mathrm{N}_2} e_v + \zeta_v Q_{\mathrm{J}}^e + \frac{1}{\tau_{vt}} \rho_{\mathrm{N}_2} (e_v^0 - e_v) \end{bmatrix} \tag{15}$$

where W_k corresponds to the mass production per unit volume of the kth species due to chemical reactions, with the chemical reactions taking place in air taken from Refs. [35,39–43] as outlined in Table 1. The chemical reactions include Townsend ionization, electron–ion recombination, ion–ion recombination, electron attachment, electron beam ionization, and nitrogen and oxygen dissociation. In determining the reduced electric field needed for the Townsend ionization rates when the plasma is in the presence of a strong externally applied magnetic field, it is important to use the electric field in the electron frame of reference instead of the laboratory or neutrals reference frame. A justification for doing so and details on how to find iteratively the electric field in the charged species reference frame can be found in the appendix of Ref. [36].

In addition, e_v^0 stands for the nitrogen vibration energy at equilibrium, which is written as a function of the characteristic vibrational temperature of nitrogen (as in Ref. [47]) with the latter set to 3353 K as suggested in [48]. Further, the fraction of the Joule heating that is consumed in the excitation of the vibration levels of the nitrogen molecule ζ_v is as specified in [45,46] as outlined in Table 2, while the vibration-translation relaxation time τ_{vt} is taken here from [49,29],

$$\frac{1}{\tau_{vt}} = 7 \cdot 10^{-16} \cdot N \cdot \exp(-141 \cdot T^{-1/3}) + 5 \cdot 10^{-18} \cdot N_{\mathrm{O}} \cdot \exp(-128 \cdot T^{-1/2}) \tag{16}$$

with τ_{vt} in seconds, N in meters^{-3}, and T in Kelvin. The latter correlation for the nitrogen vibrational relaxation time is preferred to the more commonly used Millikan correlation because it is significantly more accurate at the low temperatures typically encountered in plasma aerodynamics.

Two other terms appearing within the source vector $\boldsymbol{S}$ that need to be specified are the electron species Joule heating, which can be derived from basic principles to become (see the Appendix)

$$Q_J^e = \frac{|C_e| N_e}{\mu_e} |\boldsymbol{V}^e - \boldsymbol{V}^n|^2 \tag{17}$$

and the turbulence kinetic energy production term Q_k, which can be shown to be equal to [50]

$$Q_k = \sum_{i=1}^3 \sum_{j=1}^3 \left[\eta_{\mathrm{t}} \left(\frac{\partial \boldsymbol{V}_i^n}{\partial x_j} + \frac{\partial \boldsymbol{V}_j^n}{\partial x_i} - \frac{2}{3}\delta_{ij} \sum_{k=1}^3 \frac{\partial \boldsymbol{V}_k^n}{\partial x_k} \right) - \frac{2}{3}\delta_{ij}\rho k \right] \frac{\partial \boldsymbol{V}_i^n}{\partial x_j} \tag{18}$$

Also needed within the coupled system Eq. (10) are the vectors $\boldsymbol{Y}$ and $\boldsymbol{H}$,

Table 1 Eight-species, 28-reactions air chemical model used for all test cases shown herein[a]

No.	Reaction	Rate coefficient	References
1a	$e^- + N_2 \rightarrow N_2^+ + e^- + e^-$	$\exp(-0.0105809 \cdot \ln^2 E^\star - 2.40411 \cdot 10^{-75} \cdot \ln^{46} E^\star)$ cm^3/s	[35]
1b	$e^- + O_2 \rightarrow O_2^+ + e^- + e^-$	$\exp(-0.0102785 \cdot \ln^2 E^\star - 2.42260 \cdot 10^{-75} \cdot \ln^{46} E^\star)$ cm^3/s	[35]
2a	$e^- + O_2^+ \rightarrow O + O$	$2.0 \cdot 10^{-7} \cdot (300/T_e)^{0.7}$ cm^3/s	[39]
2b	$e^- + N_2^+ \rightarrow N + N$	$2.8 \cdot 10^{-7} \cdot (300/T_e)^{0.5}$ cm^3/s	[40]
3a	$O_2^- + N_2^+ \rightarrow O_2 + N_2$	$2.0 \cdot 10^{-7} \cdot (300/T)^{0.5}$ cm^3/s	[40]
3b	$O_2^- + O_2^+ \rightarrow O_2 + O_2$	$2.0 \cdot 10^{-7} \cdot (300/T)^{0.5}$ cm^3/s	[40]
4a	$O_2^- + N_2^+ + N_2 \rightarrow O_2 + N_2 + N_2$	$2.0 \cdot 10^{-25} \cdot (300/T)^{2.5}$ cm^6/s	[40]
4b	$O_2^- + O_2^+ + N_2 \rightarrow O_2 + O_2 + N_2$	$2.0 \cdot 10^{-25} \cdot (300/T)^{2.5}$ cm^6/s	[40]
4c	$O_2^- + N_2^+ + O_2 \rightarrow O_2 + N_2 + O_2$	$2.0 \cdot 10^{-25} \cdot (300/T)^{2.5}$ cm^6/s	[40]
4d	$O_2^- + O_2^+ + O_2 \rightarrow O_2 + O_2 + O_2$	$2.0 \cdot 10^{-25} \cdot (300/T)^{2.5}$ cm^6/s	[40]
5a	$e^- + O_2 + O_2 \rightarrow O_2^- + O_2$	$1.4 \cdot 10^{-29} \cdot (300/T_e) \cdot \exp(-600/T) \cdot \exp(700 \cdot (T_e - T)/(T_e T))$ cm^6/s	[40]
5b	$e^- + O_2 + N_2 \rightarrow O_2^- + N_2$	$1.07 \cdot 10^{-31} \cdot (300/T_e)^2 \cdot \exp(-70/T) \cdot \exp(1500 \cdot (T_e - T)/(T_e T))$ cm^6/s	[40]
6	$O_2^- + O_2 \rightarrow e^- + O_2 + O_2$	$8.6 \cdot 10^{-10} \cdot \exp(-6030/T)(1 - \exp(-1570/T))$ cm^6/s	[41], Ch. 2
7a	$O_2 \rightarrow e^- + O_2^+$	$2.0 \cdot 10^{17} \cdot Q_b^\star$ 1/s	[42]
7b	$N_2 \rightarrow e^- + N_2^+$	$1.8 \cdot 10^{17} \cdot Q_b^\star$ 1/s	[42]
8a	$O_2 + O_2 \rightarrow 2O + O_2$	$3.7 \cdot 10^{-8} \cdot \exp(-59380/T)(1 - \exp(-2240/T))$ cm^3/s	[43], [39]
8b	$O_2 + N_2 \rightarrow 2O + N_2$	$9.3 \cdot 10^{-9} \cdot \exp(-59380/T)(1 - \exp(-2240/T))$ cm^3/s	[43], [39]
8c	$O_2 + O \rightarrow 3O$	$1.3 \cdot 10^{-7} \cdot \exp(-59380/T)(1 - \exp(-2240/T))$ cm^3/s	[43], [39]
8d	$N_2 + O_2 \rightarrow 2N + O_2$	$5.0 \cdot 10^{-8} \cdot \exp(-113200/T)(1 - \exp(-3354/T))$ cm^3/s	[43], [39]
8e	$N_2 + N_2 \rightarrow 2N + N_2$	$5.0 \cdot 10^{-8} \cdot \exp(-113200/T)(1 - \exp(-3354/T))$ cm^3/s	[43], [39]
8f	$N_2 + O \rightarrow 2N + O$	$1.1 \cdot 10^{-7} \cdot \exp(-113200/T)(1 - \exp(-3354/T))$ cm^3/s	[43], [39]
9a	$O + O + O_2 \rightarrow 2O_2$	$2.45 \cdot 10^{-31} \cdot T^{-0.63}$ cm^6/s	[43], [39]
9b	$O + O + N_2 \rightarrow O_2 + N_2$	$2.76 \cdot 10^{-34} \cdot \exp(720/T)$ cm^6/s	[43], [39]
9c	$O + O + O \rightarrow O_2 + O$	$8.8 \cdot 10^{-31} \cdot T^{-0.63}$ cm^6/s	[43], [39]
9d	$N + N + O_2 \rightarrow N_2 + O_2$	$8.27 \cdot 10^{-34} \cdot \exp(500/T)$ cm^6/s	[43], [39]
9e	$N + N + N_2 \rightarrow 2N_2$	$8.27 \cdot 10^{-34} \cdot \exp(500/T)$ cm^6/s	[43], [39]
9f	$N + N + O \rightarrow N_2 + O$	$8.27 \cdot 10^{-34} \cdot \exp(500/T)$ cm^6/s	[43], [39]
9g	$N + N + N \rightarrow N_2 + N$	$8.27 \cdot 10^{-34} \cdot \exp(500/T)$ cm^6/s	[43], [39]

[a]Notation and units: $E^\star$ is the reduced effective electric field in the electron reference frame ($E^\star \equiv |\boldsymbol{E} + \boldsymbol{V}^e \times \boldsymbol{B}|/N$) in units of $V \cdot m^2$; T_e is the electron temperature in Kelvin; T is the neutrals temperature in Kelvin; and $Q_b^\star$ is the ratio in Watts between the electron beam power per unit volume Q_b and the total number density of the plasma N ($Q_b^\star \equiv Q_b/N$).

$$\boldsymbol{Y}_i = \begin{bmatrix} \beta_1^+ \boldsymbol{E}_i - \beta_1^- \boldsymbol{J}_i \\ \vdots \\ \beta_{n_s}^+ \boldsymbol{E}_i - \beta_{n_s}^- \boldsymbol{J}_i \\ 0 \\ \vdots \\ 0 \end{bmatrix}^D \quad \boldsymbol{H} = \begin{bmatrix} \rho_1 \mu_1 \left(\beta_1^+ + \frac{1}{\sigma}\beta_1^-\right) \\ \vdots \\ \rho_{n_s} \mu_{n_s} \left(\beta_{n_s}^+ + \frac{1}{\sigma}\beta_{n_s}^-\right) \\ 0 \\ \vdots \\ 0 \end{bmatrix} \tag{19}$$

where the charged species mobilities μ_k are a function of total number density, species temperature, and reduced electric field. Expressions for the charged species mobilities in dry air can be found in Ref. [35]. The electron temperature needed to obtain the mobility, the effective pressure, the specific enthalpy, and the specific internal energy of the electron species is obtained here through the local approximation by assuming that the electron temperature is a function of the local reduced electric field and does not depend on its gradients in space or time. This can be shown to yield an expression for T_e function of $E^\star$, as outlined in Table 3. This is generally accepted to yield a good approximation of the electron temperature except within the cathode sheath. Such is not a cause of concern, however, because the latter is primarily ion dominated and does not depend too significantly on electron temperature for many problems of interest.

yield similar results when using explicit schemes to integrate the governing equations. However, when using an implicit scheme as done herein, it is important to use smooth polynomials to obtain optimal convergence rates. Should we interpolate through the raw data instead of using polynomials, the derivatives within the Jacobians could change abruptly from one time step to the other, and this could lead to slower convergence or even convergence hangs.

Three more matrices that are needed within the coupled governing equations are the matrix D,

$$[D_i]_{k,r} = \begin{cases} \alpha_{kr} \boldsymbol{\Delta} \boldsymbol{V}_i^r + (\alpha_{kr} - \delta_{kr}) \boldsymbol{V}_i^n & \text{if } k \le n_{\text{cs}} \text{ and } r \le n_{\text{cs}} \\ \frac{1}{e_i^\star} \sum_{m=1}^{n_{\text{cs}}} w_m h_m (\boldsymbol{V}_i^m - \boldsymbol{V}_i^n) & \text{if } k = r = n_s + 4 \\ 0 & \text{otherwise} \end{cases} \tag{20}$$

the matrix Z related to the unsteady terms,

$$[Z]_{k,r} = \begin{cases} \alpha_{kr} & \text{if } k \le n_s \text{ and } r \le n_s \\ \delta_{kr} & \text{otherwise} \end{cases} \tag{21}$$

and the diffusion matrix K, which includes the Navier–Stokes shear stresses as well as all second derivatives except for electron temperature gradients,

$$[K_{ij}]_{k,r} = \begin{cases} \delta_{ij}\left(\delta_{kr}\nu_k^\star \beta_k^n + \frac{1}{|C_r|}\mu_r k_B T_r \alpha_{kr} \beta_k^c \beta_r^c\right) & \text{if } k \le n_s \text{ and } r \le n_s \\ \delta_{ij} \sum_{m=1}^{n_s} \frac{1}{|C_m|} \beta_m^i \beta_k^c \mu_m k_B \rho_m \alpha_{km} & \text{if } k \le n_s \text{ and } r = n_s + 4 \\ [\psi_{ij}]_{k-n_s, r-n_s} \eta^\star & \text{if } n_s < k \le n_s + 3 \text{ and } n_s < r \le n_s + 3 \\ \delta_{ij}(h_r + e_v \delta_{rz}) \nu_r^\star \beta_r^n & \text{if } k = n_s + 4 \text{ and } r \le n_s \\ \sum_{m=1}^{3} [\psi_{ij}]_{m, r-n_s} \eta^\star \boldsymbol{V}_m^n & \text{if } k = n_s + 4 \text{ and } n_s < r \le n_s + 3 \\ \delta_{ij}\kappa^\star & \text{if } k = n_s + 4 \text{ and } r = n_s + 4 \\ \delta_{ij}\eta_k^\star & \text{if } k = n_s + 4 \text{ and } r = n_s + 5 \\ \delta_{ij}\kappa_v^\star & \text{if } k = n_s + 4 \text{ and } r = n_s + 7 \\ \delta_{ij}\eta_k^\star & \text{if } k = n_s + 5 \text{ and } r = n_s + 5 \\ \delta_{ij}\eta_\omega^\star & \text{if } k = n_s + 6 \text{ and } r = n_s + 6 \\ \delta_{ij}\kappa_v^\star & \text{if } k = n_s + 7 \text{ and } r = n_s + 7 \\ \delta_{ij}\nu_{N_2}^\star e_v & \text{if } k = n_s + 7 \text{ and } r = z \\ 0 & \text{otherwise} \end{cases} \tag{22}$$

It is preferred to use polynomials fits to find η_v and T_e rather than interpolate through the raw data directly as was done in previous simulations of weakly ionized plasmas. Using either strategy would

where z is the row number of the N_2 mass conservation flux and where ψ_{ij} is a tensor related to the Navier–Stokes stresses that can be shown to be equal to

$$[\psi_{ij}]_{k,r} = \delta_{ij}\delta_{kr} + \delta_{ki}\delta_{rj} - (2/3)\delta_{kj}\delta_{ri} \tag{23}$$

Table 2 Polynomial coefficients needed for the fraction of energy consumed in the excitation of vibration levels of the nitrogen molecule, $\zeta_v = \sum_{n=0}^{10} k_n T_e^n$[a,b,c]

Coefficient	Value
k_0	+1.8115947E − 3
k_1	+2.1238526E − 5
k_2	−2.2082300E − 8
k_3	+7.3911515E − 12
k_4	−8.0418868E − 16
k_5	+4.3999729E − 20
k_6	−1.4009604E − 24
k_7	+2.7238062E − 29
k_8	−3.1981279E − 34
k_9	+2.0887979E − 39
k_{10}	−5.8381036E − 45

[a]The expression for ζ_v can be used in the range $0 < T_e < 60{,}000$ K.
[b]The polynomial approximates the experimental data in [45] and Chap. 21 of [46].
[c]T_e is in Kelvin.

Table 3 Polynomial coefficients needed to determine the electron temperature, $T_e = \max\{T, \exp[\sum_{n=0}^{8} k_n (\ln E^\star)^n]\}$[a,b,c]

Coefficient	Value
k_0	−3.691675326924958825 11E + 08
k_1	−6.269567137477126717 57E + 07
k_2	−4.655284906078055500 98E + 06
k_3	−1.973944482887396879 96E + 05
k_4	−5.227846628970892197 69E + 03
k_5	−8.855456178745656359 30E + 01
k_6	−9.369147379233638828 21E − 01
k_7	−5.660733944210671712 84E − 03
k_8	−1.495358826913308324 94E − 05

[a]The expression for T_e can be used in the range $0 < E^\star < 3 \times 10^{-19}$ Vm^2.
[b]The polynomial approximates the experimental data in Chap. 21 of [46].
[c]$E^\star$ is in Vm^2, T_e in Kelvin, T in Kelvin.

In the latter, the molecular thermal conductivity for the neutrals κ is determined from the Mason and Saxena relation and polynomials obtained from [51], while the neutrals viscosity η and the molecular diffusion ν_k are determined from Wilke's mixing rule with polynomials for each species found in [51].

IV. Surface Boundary Conditions

While the flow properties at the inflow and outflow conditions can be specified similarly as in nonionized aerodynamics, special care must be taken in applying the boundary conditions at the surfaces of dielectrics and electrodes. For the charged species partial densities, here we follow the boundary conditions for a weakly ionized plasma specified in [35]. Specifically, for dielectrics or for $E_\chi < 0$, the following boundary condition is imposed:

$$\frac{\partial}{\partial\chi}N_+\boldsymbol{V}_\chi^+ = 0, \qquad N_- = 0, \qquad N_e = \frac{\gamma}{\mu_e}\sum_{k=1}^{n_s} N_k\mu_k\beta_k^+ \tag{24}$$

whereas for conductors and for $E_\chi \geq 0$, the following boundary condition is imposed:

$$N_+ = 0, \qquad \frac{\partial}{\partial\chi}N_-\boldsymbol{V}_\chi^- = 0, \qquad \frac{\partial}{\partial\chi}N_e\boldsymbol{V}_\chi^e = 0 \tag{25}$$

where χ is a coordinate perpendicular to the surface and pointing toward the fluid and γ is the secondary emission coefficient typically set to 0.1. In addition, $\boldsymbol{E}_\chi$ is the component of the electric field in the direction of χ, while the subscripts/superscripts $+$, $-$, and e refer to the position ions, negative ions, and electrons, respectively. Meanwhile, because the neutrals mass fractions must not exhibit a gradient perpendicular to the surfaces, the following must hold:

$$\beta_k^n\frac{\partial}{\partial\chi}w_k = 0 \tag{26}$$

Further, the total density of the mixture must be such that there is no gradient of the effective pressure including turbulence kinetic energy and electron energy contributions:

$$\frac{\partial}{\partial\chi}P^\star = 0 \tag{27}$$

In addition, on the surface nodes, the bulk mixture temperature T is fixed to a user-specified constant, and the velocity of the neutrals is fixed to zero. Regarding the boundary condition for vibrational temperature, the vibrational accommodation coefficient depends on the surface material and temperature. At $T = 300$ K, the vibrational accommodation coefficient for nitrogen on any dielectric, semiconductor, or metallic surface is quite low, on the order of 0.001 to 0.01 [52,53]. Therefore, in the first approximation, we can assume that the vibrational accommodation coefficient is equal to zero, which leads to the following boundary condition:

$$\frac{\partial}{\partial\chi}T_v = 0 \tag{28}$$

To close the system of equations at the surface nodes, we need two more equations for the turbulence kinetic energy and its dissipation rate. Because the $k\omega$ turbulence model is integrated here through the entire boundary layer including the laminar sublayer, we should not use wall functions but rather fix the turbulence kinetic energy and its specific dissipation rate to their asymptotic expressions assuming that the surface is smooth [38],

$$k = 0 \tag{29}$$

$$\omega = \frac{36}{5}\frac{\eta}{\rho(\Delta\chi)^2} \tag{30}$$

where $\Delta\chi$ is the distance between the wall node and its nearest inner node.

The boundary conditions needed to obtain $\boldsymbol{U}$ at the surface nodes as outlined in this section can be applied to either electrodes or dielectrics. Further, on the dielectrics, the potential is specified such that no current flows perpendicular to the surface. This can be shown to yield the following:

$$\frac{\partial\phi}{\partial\chi} = -\frac{1}{\sigma}\sum_{k=1}^{n_{\rm cs}} s_k\mu_k\frac{\partial P_k}{\partial\chi} \quad \text{for dielectrics only} \tag{31}$$

Although the latter is only valid in the steady-state regime for which the charge accumulation on the dielectric surface does not vary in time, the rate of change of the charge accumulation can be taken into account by varying the potential on the dielectric surface as specified in [54].

It is noted that the expressions presented in this section were derived assuming no external magnetic field. However, they remain valid in the presence of a magnetic field following the strategy outlined in [36] by setting the magnetic field vector to zero at the boundary and near-boundary nodes.

V. Discretization Stencils

Some of the derivatives within the system of equations comprising the recast drift-diffusion model and the Favre-averaged Navier–Stokes outlined in Eq. (10) are commonly encountered in aerodynamics and can be discretized using standard stencils. For instance, the convection derivative $\partial\boldsymbol{F}_i/\partial x_i$ is discretized through the Roe flux difference splitting scheme [55] turned second-order accurate through the centered Yee limiters [56] and using eigenvectors and eigenvalues similar to those outlined in the appendix of [57] but with modifications for a real gas with multiple species including the turbulence kinetic energy and the nitrogen vibrational energy in nonequilibrium. In addition, the second derivative $\partial/\partial x_j(K_{ij}\partial\boldsymbol{G}/\partial x_i)$ is discretized using centered stencils as such does not lead to spurious oscillations.

On the other hand, other derivatives within Eq. (10) such as $\boldsymbol{Y}_i\partial\boldsymbol{H}/\partial x_i$ and $\partial D_i\boldsymbol{U}/\partial x_i$ are not commonly encountered and require nonstandard discretization stencils. To obtain monotonic solutions, the term $\boldsymbol{Y}_i\partial\boldsymbol{H}/\partial x_i$ is discretized, following the approach specified in [33], and the term $\partial D_i\boldsymbol{U}/\partial x_i$ is discretized using a flux vector splitting approach of the form

$$(D_i\boldsymbol{U})^{X_i+1/2} = (D_i^+)^{X_i}\boldsymbol{U}^{X_i} + (D_i^-)^{X_i+1}\boldsymbol{U}^{X_i+1} \tag{32}$$

which is turned second-order accurate through upwinded Total Variation Diminishing minmod limiters. In Eq. (32), the matrix $D_i^\pm$ corresponds to

$$[D_i^\pm]_{k,r} = \begin{cases} 0.5[D_i]_{k,k} \pm 0.5\,\max(\beta_k^c\zeta_D a, |[D_i]_{k,k}|) & \text{if } r = k \\ [D_i]_{k,r}([D_i^\pm]_{r,r} - [D_i^\pm]_{k,k})/([D_i]_{r,r} - [D_i]_{k,k}) & \text{if } k \leq n_{\rm cs} \quad \text{and} \quad r \leq n_{\rm cs} \quad \text{and} \quad r \neq k \\ [D_i]_{k,r} & \text{otherwise} \end{cases} \tag{33}$$

It can be easily demonstrated that the latter becomes the Steger–Warming scheme if only one type of negative species is present (i.e., if the plasma has no negative ions). When more than one type of negative species is present, the latter formulation for $D_i^{\pm}$ will still result in $D_i^+ + D_i^- = D_i$, a necessary condition for a well-posed flux vector splitting scheme. It could be argued that the use of a Steger–Warming-like stencil leads to excessive dissipation within viscous layers and hence prevents boundary layers to be resolved with high resolution. However, this is only the case if it is used to discretize the term $\partial \boldsymbol{F}_i/\partial x_i$. When discretizing the term $\partial D_i \boldsymbol{U}/\partial x_i$, the use of flux vector splitting does not lead to a low resolution of viscous layers.

In addition, because electron temperature is a function of the reduced electric field, which is itself a function of potential gradients, the second derivatives of the electron temperature within the potential equation yield third derivatives in the potential. Taking the latter into consideration, it can be demonstrated that, should centered discretization stencils be used for the electron temperature derivatives, the discretization equation for the potential equation would not be monotonicity preserving and hence could lead to spurious oscillations. To prevent even–odd discoupling of the potential, it can be shown that the electron temperature derivatives should be upwinded in the direction of the electric field. The stencil that we are proposing for this purpose is thus

$$(\delta_{x_i} T_e)^{X_i+1/2} = \frac{1}{\Delta x_i} \frac{\left[\left(T_e^{X_i+1/2} - T_e^{X_i-1/2}\right)\left(|\boldsymbol{E}_i^{X_i}| + \boldsymbol{E}_i^{X_i} + E_{\text{div}}\right) + \left(T_e^{X_i+3/2} - T_e^{X_i+1/2}\right)\left(|\boldsymbol{E}_i^{X_i+1}| - \boldsymbol{E}_i^{X_i+1} + E_{\text{div}}\right)\right]}{\left(|\boldsymbol{E}_i^{X_i}| + |\boldsymbol{E}_i^{X_i+1}| + 2E_{\text{div}}\right)} \tag{34}$$

where E_{div} is a small user-specified constant that is typically set to 10 V/m and that is needed to prevent a division by zero. The latter discretization stencil needs to be applied not only to the electron temperature gradient terms within the potential equation but also to the electron temperature gradient terms within the charged species transport equations. On the other hand, the electron temperature gradient terms within the total energy equation can be discretized using centered stencils as they do not lead to any problem.

Another term that needs special consideration upon discretizing the equations is the magnitude of the electric field used to calculate the electron temperature using the local approximation. To prevent even–odd node discoupling, it is found necessary to apply a smoothing operator as follows:

$$|\boldsymbol{E}^e| = \frac{1}{n_d} \sum_{i=1}^{n_d} \Big[(1/6)(|\boldsymbol{E}^e|^{X_i-3/2})^{0.4} + (1/3)(|\boldsymbol{E}^e|^{X_i-1/2})^{0.4} + (1/3)(|\boldsymbol{E}^e|^{X_i+1/2})^{0.4} + (1/6)(|\boldsymbol{E}^e|^{X_i+3/2})^{0.4} \Big]^{1/0.4} \tag{35}$$

Note that the latter smoothing operator is only used when determining the electron temperature from the effective electric field in the electron reference frame. When needed to compute the Townsend ionization chemical source terms (i.e., reactions 1a and 1b in Table 1), the effective electric field at a given node is computed by taking the minmod of the electric field on the nearby interfaces as specified in Eq. (53) in [35].

VI. Generalized Coordinates

To tackle problems in which the mesh becomes nonorthogonal when body fitted, the proposed coupled drift-diffusion and Navier–Stokes system outlined in the previous section can be converted from Cartesian to generalized "curvilinear" coordinates following the conservative method of Viviand [58] and Vinokur [59]. After some algebra, it can be demonstrated that, in generalized coordinates, the coupled system Eq. (10) becomes

$$Z\frac{\partial \boldsymbol{U}^\star}{\partial t} + \sum_{i=1}^{3} \frac{\partial \boldsymbol{F}_i^\star}{\partial X_i} + \sum_{i=1}^{3} \frac{\partial}{\partial X_i} D_i^\star \boldsymbol{U}^\star - \sum_{i=1}^{3}\sum_{j=1}^{3} \frac{\partial}{\partial X_i}\left(K_{ij}^\star \frac{\partial \boldsymbol{G}}{\partial X_j}\right) + \sum_{i=1}^{3} \boldsymbol{Y}_i^\star \frac{\partial \boldsymbol{H}}{\partial X_i} = \boldsymbol{S}^\star \tag{36}$$

where $\boldsymbol{U}^\star = \Omega \boldsymbol{U}$, where $\boldsymbol{S}^\star = \Omega \boldsymbol{S}$ and where

$$\boldsymbol{F}_i^\star = \Omega \sum_{m=1}^{3} X_{i,m} \boldsymbol{F}_m \tag{37}$$

$$\boldsymbol{Y}_i^\star = \Omega \sum_{m=1}^{3} X_{i,m} \boldsymbol{Y}_m \tag{38}$$

$$D_i^\star = \sum_{m=1}^{3} X_{i,m} D_m \tag{39}$$

$$K_{ij}^\star = \Omega \sum_{m=1}^{3}\sum_{n=1}^{3} X_{j,m} X_{i,n} K_{mn} \tag{40}$$

In addition, any spatial derivative that appears within the source term vector $\boldsymbol{S}^\star$ is rewritten as

$$\frac{\partial}{\partial x_i}(\cdot) = \sum_{m=1}^{3} X_{m,i} \frac{\partial}{\partial X_m}(\cdot) \tag{41}$$

In the latter, Ω stands for the inverse of the metric Jacobian, while $X_{i,j}$ stands for the partial derivative of X_i with respect to x_j. Expressions for these two terms in two and three dimensions can be found in the appendix of Ref. [57].

VII. Block-Implicit Integration

The system of transport equations presented earlier consists of the charged species transport equations along with the neutrals mass, momentum, and energy equations in coupled form. Integrating such a system of equations must be done with care as it involves a large disparity between the physical time scales. Should an explicit integration strategy be used, the integration step length would have to be set to excessively small values to prevent divergence toward aphysical states. Using a scalar implicit method (i.e., integrating implicitly the transport equations sequentially keeping the others frozen) would also lead to some difficulties due to the strong dependence between the transport equations. Rather, to enable the use of aerodynamic-scale integration step lengths, it is found necessary to integrate all transport equations conjunctly through a block-implicit method as is commonly done when solving chemically reacting flows.

For this purpose, it is necessary to first derive the delta form of the governing equations. Such can be done starting from Eq. (36) evaluated at the pseudotime level $n+1$, adding a pseudotime derivative, and subtracting/adding the discretized residual evaluated at pseudotime level n. We thus obtain the delta form of the governing equations:

$$\Gamma^n \Delta^n \boldsymbol{U}^\star + \sum_{i=1}^{n_d} \left[\delta_{X_i} \Delta^n \boldsymbol{F}_i^\star + \delta_{X_i} \Delta^n (D_i^\star \boldsymbol{U}^\star) + \Delta^n (\boldsymbol{Y}_i^\star \delta_{X_i} \boldsymbol{H}) - \sum_{j=1}^{n_d} \delta_{X_i} \Delta^n (K_{ij}^\star \delta_{X_j} \boldsymbol{G}) \right]$$
$$- \Delta^n \boldsymbol{S}^\star + \Delta^n (Z \delta_t \boldsymbol{U}^\star) = -\boldsymbol{R}_\Delta^n \tag{42}$$

The latter equation involves solving a large banded matrix, which would require too much computer memory storage and CPU time for multidimensional problems. One alternative is to approximate the delta form with a multiplication of one-dimensional operators, a technique usually referred to as approximate factorization [60,61] or alternate direction implicit (ADI). However, contrarily to the scalar approximate factorization in [60], we apply here the approximate factorization to the matrix form of the equations (as opposed to each scalar equation independently of the others), hence resulting in a block implicit method (see [62,63] pp. 318–319] for a discussion of block-implicit algorithms):

$$\left\{ \prod_{i=1}^{n_d} \left[I + (\Gamma^n)^{-1} \delta_{X_i} \left(\frac{\partial \boldsymbol{F}_i^\star}{\partial \boldsymbol{U}^\star} \right)^n + (\Gamma^n)^{-1} \delta_{X_i} D_i^{\star n} \right. \right.$$
$$+ (\Gamma^n)^{-1} Y_i^{\star n} \delta_{X_i} \left(\frac{\partial \boldsymbol{H}}{\partial \boldsymbol{U}^\star} \right)^n$$
$$- (\Gamma^n)^{-1} \sum_{j=1}^{n_d} \delta_{X_i} \left(K_{ij}^\star \delta_{X_j} \frac{\partial \boldsymbol{G}}{\partial \boldsymbol{U}^\star} \right)^n - \delta_{1i} (\Gamma^n)^{-1} \left(\frac{\partial \boldsymbol{S}^\star}{\partial \boldsymbol{U}^\star} \right)^n$$
$$\left. \left. + \delta_{1i} (\Gamma^n)^{-1} Z^n \left(\frac{\partial (\delta_t \boldsymbol{U}^\star)}{\partial \boldsymbol{U}^\star} \right)^n \right] \right\} \Delta^n \boldsymbol{U}^\star = -(\Gamma^n)^{-1} \boldsymbol{R}_\Delta^n \tag{43}$$

For $K^\star$, $\boldsymbol{Y}^\star$, Z, and $D^\star$ frozen within one iteration, Eq. (43) corresponds to Eq. (42) if, when the multiplication is expanded, all terms involving $(\Gamma^n)^{-2}$ or $(\Gamma^n)^{-3}$ are neglected. Such is a valid approximation as long as the pseudotime step used within the preconditioning matrix remains relatively small.

It is noted that the linearization matrices and the difference operators within Eq. (43) are for the most part symbolic. For instance, $\delta_{X_i} D_i^{\star n}$ stands for the linearized form of the flux vector splitting discretization outlined in Eq. (32), while $\partial \boldsymbol{F}_i^\star / \partial \boldsymbol{U}^\star$ stands for the Jacobians involved in the linearization of the Roe flux difference splitting scheme. Similarly, the linearization matrix $\partial \boldsymbol{S}^\star / \partial \boldsymbol{U}^\star$ does not include the derivatives of all terms within the source term vector $\boldsymbol{S}$ with respect to the vector of conserved variables $\boldsymbol{U}$. Specifically, while all chemical reactions are linearized, the Townsend ionization rates are linearized here under the condition of constant current for higher stability [35]. Other source terms within $\boldsymbol{S}$ that must not be linearized for stability purposes are the temperature gradients, the turbulence kinetic energy production term, the Coulomb and Lorentz body forces, and the positive terms part of $\beta_k^+ \mu_k \rho_k \rho_c / \epsilon_0$ (see Sec. 7 in [35] for more details).

Within the delta form, the preconditioning matrix Γ is set equal to

$$\Gamma = \frac{1}{\Delta \tau} \begin{bmatrix} [\beta_1^n + \zeta_\Gamma^i \beta_1^i + \beta_1^e \min(\zeta_\Gamma^i, \zeta_\Gamma^e / \alpha_{ee})]^{-1} \\ \vdots \\ [\beta_{n_s}^n + \zeta_\Gamma^i \beta_{n_s}^i + \beta_{n_s}^e \min(\zeta_\Gamma^i, \zeta_\Gamma^e / \alpha_{ee})]^{-1} \\ 1 \\ \vdots \\ 1 \end{bmatrix}^D \tag{44}$$

where ζ_Γ^i and ζ_Γ^e are user-defined constants typically set to 0.1 and 0.001, respectively. Setting the local pseudotime step $\Delta\tau$ equal to the minimum Courant-Friedrichs-Lewy (CFL) condition as is often done would lead to slow convergence of the viscous terms within the laminar sublayer of the turbulent boundary layer due to the high aspect ratio of the grid cells in that region. Here, we rather set the pseudotime step to the geometric average between the maximum and the minimum CFL conditions within all dimensions:

$$\Delta \tau = \mathrm{CFL} \min_{i=1}^{3} \left(\frac{\Delta x_i}{|\boldsymbol{V}_i^n| + a} \right)^{0.5} \max_{i=1}^{3} \left(\frac{\Delta x_i}{|\boldsymbol{V}_i^n| + a} \right)^{0.5} \tag{45}$$

Taking the geometric average between the maximum and minimum CFL conditions keeps the local pseudotime step within high aspect ratio cells to a value that, while being lower than in cells with an aspect ratio of 1, is not so low as to induce slow convergence. It is noted that, should the viscous terms $\partial / \partial X_i (K_{ij}^\star \partial / \partial X_j \boldsymbol{G})$ not be linearized and treated in a fully implicit manner as done herein, they would lead to stability issues should the pseudotime step be set significantly higher than the minimum CFL condition. But because the viscous terms are treated here in a fully implicit manner by avoiding spatial derivatives within the Jacobians (as is common in other compressible flow codes), they do not lead to stability issues at any CFL number, and this permits us to set the local pseudotime step higher than usual within high aspect ratio cells, hence leading to faster convergence.

Effectively, the preconditioner Γ is such that within regions of quasi neutrality or within the anode sheath the electrons would be subject to the same pseudotime step as the ions (i.e., $\zeta_\Gamma^i \Delta\tau$). Within the cathode sheath, however, the pseudotime step of the electrons is progressively decreased until it reaches the value $\zeta_\Gamma^e \Delta\tau$ near the cathode. At least for the problems shown hereafter, such is found to yield optimal convergence rates.

Meanwhile, for the potential equation based on Ohm's law, Eq. (9), the pseudotime step is set as suggested in [36],

$$\Delta \tau_\phi = L_c \cdot \min_{i=1}^{3} \left(\frac{\Delta x_i}{\sigma_{\mathrm{ref}} + \sigma} \right) \tag{46}$$

with L_c some characteristic length scale typically set to the average distance between the electrodes and σ_{ref} some reference conductivity typically given a value of 0.003 S/m.

While here it is considered crucial for high computational efficiency to integrate the charged species transport equations in coupled form with the neutrals transport equations, it is also found that the opposite is true with respect to the potential equation. Having experimented with both a coupled and uncoupled approach, we have found that integrating the potential equation shown in Eq. (9) in coupled form with the fluid equations outlined in Eq. (10) would result in lower, not higher, computational efficiency. This is due, in part, to the fluid transport equations (for either the neutral or charged species) not depending directly on the potential but rather on the electric field that is itself obtained from the spatial gradients of the potential. Because of this, the Jacobians of the fluid equations used within the block-implicit ADI scheme do not depend on the potential equation, and therefore their update in pseudotime is unaffected whether the potential is integrated in coupled form or not. On the other hand, integrating the potential through a separate module leads to one major advantage: several iterations of the potential can be performed for one iteration of the coupled drift-diffusion and Navier–Stokes system. For many problems, this leads to a substantial reduction in the number of iterations needed to converge the fluid transport equations and, hence, to improved computational efficiency. Indeed, the total CPU time necessary to obtain a converged solution depends strongly on the iteration count of the fluid transport equations but relatively little on the iteration count of the potential equation.

Thus, the strategy recommended (and adopted for the test cases shown in the following) is to integrate the potential equation (9) through a scalar approximate-factorization algorithm three to six times, keeping the other properties constant, followed by the integration of the fluid equations (10) through a block-implicit strategy keeping the potential constant and repeating the latter

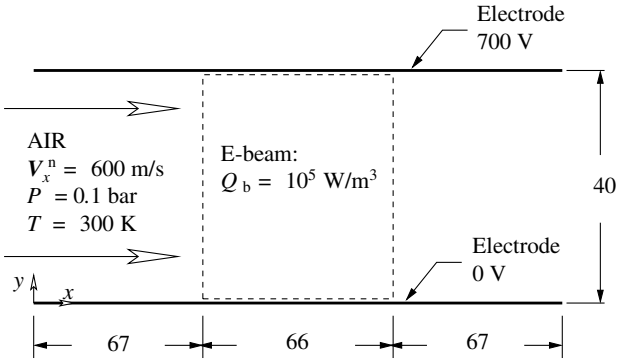

Fig. 1 Problem setup for both test cases; all dimensions in millimeters.

process until convergence is attained. As will be demonstrated through the test cases in what follows, due to the lack of stiffness of the recast computationally efficient drift-diffusion model used herein, such an approach is highly efficient and converges in more or less the same number of iterations as nonionized aerodynamics.

VIII. Code Validation

To verify the validity of the present numerical method, we solved several problems for which benchmark solutions (i.e., solutions with minimal grid-induced error) using the standard drift-diffusion model are available. For instance, we have simulated with the algorithm outlined herein the multicomponent plasma in the magnetic field test case outlined in Sec. 9.1 of [36] using the same set of chemical reactions as in [36]. Such a test case is particularly well suited to assess the validity of the implementation of the novel computationally efficient drift-diffusion model and potential equation within our aerodynamics code because it involves a weakly ionized air plasma with considerable magnetic field effects and in which the negative ions, the positive ions, and the electrons all play a significant role. When using a 360^2 mesh, the method proposed herein is seen to yield contour plots visually indiscernible from those obtained with the standard drift-diffusion model on the basis of electron density, negative and positive ion densities, and current density magnitude. This increases the confidence that the implementation of the charged species transport equations as well as of the potential equation within our aerodynamic solver is correct.

Other aspects of the present algorithm that require verification are the transport equations of the mass, momentum, and energy of the neutrals along with the transport equations of the turbulence kinetic energy and its specific dissipation rate. Such have been extensively validated through various comparisons with exact solutions and experimental data for a wide range of compressible flows in previous work (see the validation test cases in [64,65], for instance).

Further, as will be discussed in the following when analyzing the results of some test cases relevant to plasma flow control, results of sheaths obtained with our numerical method are in close agreement with those obtained through the one-dimensional drift theory of cathode sheaths outlined in [66].

Thus, because the in-house-developed plasma aerodynamics code used herein has been validated against multiple benchmark solutions, experimental results, and theoretical predictions related to both plasma sheaths and aerodynamic flows, we are fairly confident in the correctness of the computationally efficient set of equations presented in this paper as well as in its implementation within our flow solver.

IX. Test Cases

To test the capabilities of the proposed system of equations, some test cases of relevance to plasma aerodynamics are now considered. The first one consists of a glow discharge interacting with a turbulent boundary layer, and the second one corresponds to an e-beam ionized Faraday generator within a turbulent channel including the solution of the nonneutral cathode and anode sheaths. For both cases, the species consist of e^-, O_2^-, O_2^+, N_2^+, N, O, N_2, and O_2 interacting with each other according to the set of reactions outlined in Table 1.

A. Glow Discharge Interacting with Boundary Layer

The first test case considered here consists of a supersonic air flow entering a channel at a speed of 600 m/s, a temperature of 300 K, and a pressure of 10 kPa. In the middle of the channel, the air is ionized through electron beams as depicted in Fig. 1, while the potential difference between the top and the bottom walls is fixed to 700 V. On the electrodes, the secondary emission coefficient γ is set to 0.1, and the neutrals temperature is fixed to 300 K. An orthogonal mesh of 120×120 nodes is used, with some clustering near the electrodes such that the distance between the boundary and the near-boundary node is 30 μm.

Such a problem is of particular interest to plasma flow control due to the large Coulomb force induced in the boundary layer. Indeed, because the conductivity within the cathode sheath (near the bottom electrode) is much lower than within the quasi-neutral region (in the center of the domain) or in the anode sheath (near the top electrode), most of the voltage drop between the electrodes occurs within the cathode sheath. As can be seen from the electric field contours in Fig. 2, this leads to a particularly strong electric field within the cathode sheath pointing toward the wall. To satisfy Gauss's law, a change in the spatial derivative of the electric field needs to be accompanied by a net positive charge density (see Fig. 2c). Because the Coulomb force corresponds to the product of the electric field and the net charge density, this thus leads to a net force pointing toward the wall. What is particularly interesting here is that the thickness of the cathode sheath is commensurate in size with the thickness of the turbulent boundary layer. Thus, the Coulomb force acting on the neutrals due to the presence of the discharge can have an impact not only on the laminar sublayer within a few tenths of micrometers from the wall but also over most of the buffer region and outer regions of the turbulent boundary layer. Such a wall-oriented force could thus be used to prevent the boundary layer from

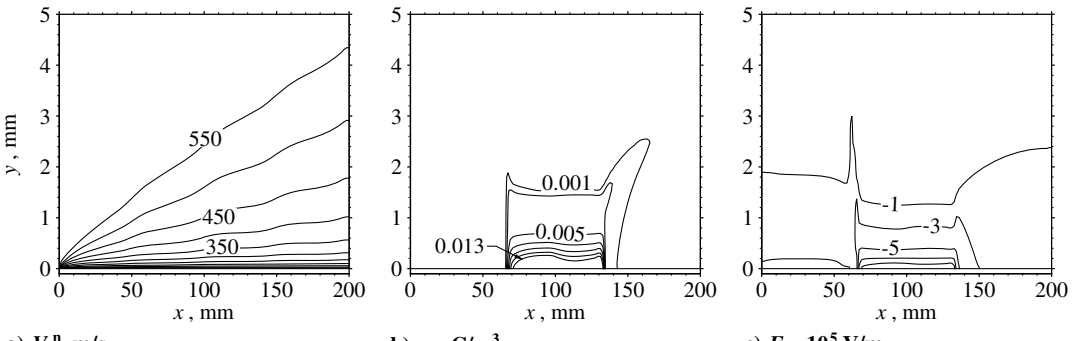

Fig. 2 Neutrals' x-velocity component, net charge density, and y component of the electric field near the cathode.

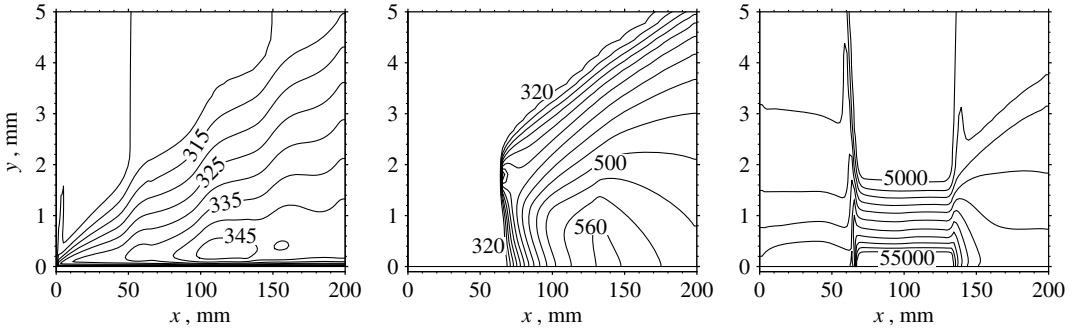

a) T b) T_v c) T_e

Fig. 3 Neutrals' temperature, vibrational temperature, and electron temperature near the cathode in Kelvin.

separating or from becoming turbulent, resulting in a significant improvement of the aerodynamic performance of the flight vehicle.

Besides being of significance to plasma aerodynamics, such a problem is particularly well suited to test the performance of our newly proposed coupled drift-diffusion and Navier–Stokes system of equations. The coupling between the drift-diffusion and the Navier–Stokes equations can best be explained as follows. Because of the Joule heating deposited within the cathode sheath is significant, it results in a change in both the nonequilibrium vibrational temperature and the bulk gas temperature, as is apparent from the temperature contours in Fig. 3. An increase in the bulk gas temperature itself results in a decrease in the number density of the plasma, affecting in the process the Townsend ionization rates, the mobilities, and the conductivity on which the charged species transport equations and potential equation depend. Thus, the electron and ion transport equations cannot be solved independently of the Navier–Stokes equations in this case because the number density of the plasma bulk is not known a priori. The Navier–Stokes equations can also not be solved independently of the charged species equations because the Joule heating distribution as well as the Coulomb force distribution is not given a priori. Rather, both sets of equations depend significantly on each other and need to be solved conjunctly.

The addition of the drift-diffusion transport equations to the neutrals mass, momentum, and total energy transport equations can be seen in Fig. 4 not to affect considerably the convergence history. Specifically, to obtain six orders of magnitude of convergence, the coupled drift-diffusion and Navier–Stokes system is seen to require only two times more iterations than the standalone Navier–Stokes system. We focus here on the first six orders of magnitude of convergence because such is generally deemed sufficient to obtain a converged solution. Further pursuing the convergence beyond six orders has been verified not to alter the solution considerably. To enable a fair comparison between both sets of equations, the user-defined CFL parameter is set initially to the same value of 0.01 for both systems and then increased to 4.0 as rapidly as permitted by the nonlinear stability restrictions (i.e., at a rate of 20% per iteration for the standalone Navier–Stokes system and at a rate of 1% per iteration for the coupled drift-diffusion and Navier–Stokes system). It is noted that, while the standalone Navier–Stokes system does include the Wilcox two-equation turbulence model and temperature-dependent

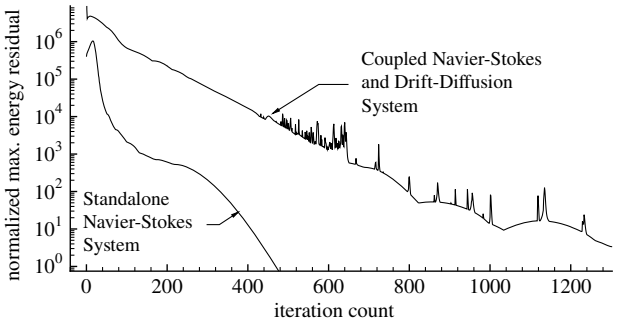

Fig. 4 Convergence histories for the glow discharge test case.

specific heats, it does differ from the coupled drift-diffusion and Navier–Stokes system on the following four points: 1) it does not include the electromagnetic forces and energy source terms in the momentum and energy transport equations; 2) it does not include the solution of the electron and ion transport equations; 3) it does not include electron beam ionization or any other chemical reaction; and 4) it is limited to the O_2 and N_2 species and does not include the other six species. Perhaps because of the considerably reduced complexity of the physical model, the standalone Navier–Stokes system exhibits faster convergence. Nonetheless, the proposed coupled drift-diffusion and Navier–Stokes system does hold its own and can be converged almost as rapidly as conventional nonionized aerodynamics for this test case.

B. Glow Discharge in Magnetic Field

We now repeat the previous test case in which a glow discharge interacts with a turbulent boundary layer but in the presence of an externally applied magnetic field. The magnetic field is oriented perpendicular to the computational domain, points in the positive z direction, and is given a magnitude of 0.25 T. Because the magnetic field vector, the current density vector, and the neutrals velocity vector are all perpendicular to each other, such a problem is of importance because it constitutes a so-called Faraday-type MHD generator that generates power through the Lorentz force.

Raising the magnetic field to values higher than the 0.25 T used herein prevents convergence to the steady state because it leads to unsteady waves propagating within the anode sheath and the quasi-neutral region. This should not be surprising. As was observed in [29], using a similar chemical model as used herein, air plasmas with the electron temperature in nonequilibrium become unsteady in the quasi-neutral region when the Hall parameter for the electrons approaches or exceeds 1. Recalling that the electron Hall parameter corresponds to the product between the electron mobility and the magnitude of the magnetic field, and noting that the electron mobility varies between 1.8 and 5 m^2/Vs within the e-beam ionized region in this case, the Hall parameter for the electrons reaches 1.2 when the magnetic field is set to 0.25 T. Raising the magnetic field to higher values would hence lead to an electron Hall parameter significantly exceeding1 and hence to unsteady behavior.

Various checks were made to ensure that the numerical solution obtained herein was free of error and was in accordance with previously obtained data. For instance, the voltage drop within the sheath near the cathode (170 V) as well as the cathode sheath thickness (0.2 mm) were verified to match those obtained through the one-dimensional exact solution outlined in [66] on page 180. In doing the latter comparison, the cathode sheath thickness was defined as the region near the cathode where the current is mostly ionic and does not include the part of the sheath where the current is mostly electronic and where ambipolar effects are significant. It was also verified that the integral of the current density is conserved from one electrode to the other as should be the case in a plasma in the steady state subject to only one electrode pair. Further, it was verified that the current density streamlines (see Fig. 5) are inclined at the angle expected at a Hall parameter of ∼0.4.

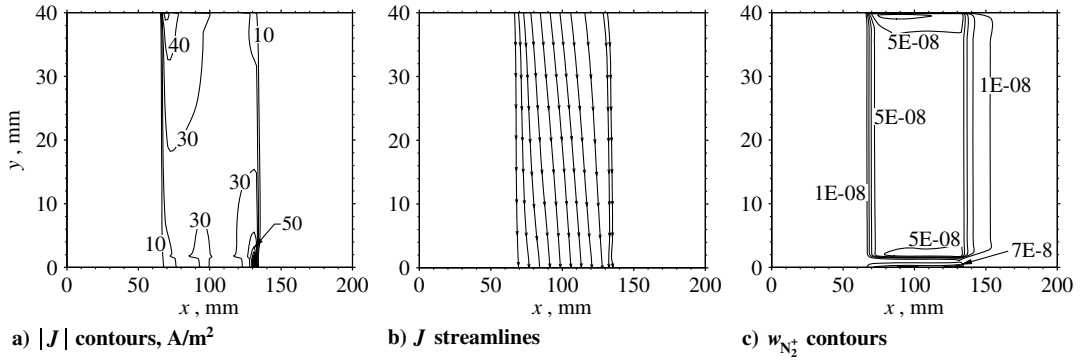

Fig. 5 Current density magnitude, current density streamlines, and N_2^+ ion mass fraction contours for the glow discharge in the magnetic field test case.

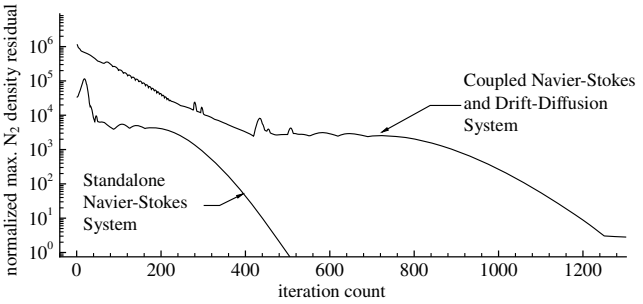

Fig. 6 Convergence histories for the glow discharge case in presence of a magnetic field.

As in the previous test case, the proposed coupled drift-diffusion and Navier–Stokes system is seen to converge five to six orders of magnitude in about 1000 iterations, which is commensurate with the number of iterations needed to converge the standalone Navier–Stokes system (see Fig. 6). Although the rate of convergence slows down when the iteration count reaches 1300 or so, such is not a particular source of concern as it is verified that iterating the system beyond this point does not lead to a significant change in the solution. The slowdown of the residual convergence history after five to six orders is not unique to this system of equations. Such is in fact commonly encountered when using approximate factorization (also known as ADI) to solve problems with a large discrepancy between the time scales originating either from the physical model or from the mesh spacing. Although this issue could perhaps be overcome through the use of other integration strategies such as Jacobian-Free Newton Krylov (JFNK), for instance, there may be difficulties in deploying the latter to a chemically reacting system of equations as used herein. Further, for many problems of interest in aerodynamics, iterating beyond four to five orders of convergence rarely changes appreciably the solution and is hence computing time wasted that could be put to better use by solving more refined meshes.

X. Conclusions

A new system of equations presented here permits for the first time the coupled integration of the electron and ion transport equations with the neutrals mass, momentum, and total energy transport equations. Such is made possible through the use of a recently developed recast of the drift-diffusion model that exhibits no stiffness (when solved with block-implicit methods) and can hence be integrated with time steps similar in size to those used to integrate nonionized aerodynamic flows. The coupled system includes nonequilibrium of the nitrogen vibrational energy and of the electron energy, real gas effects, multiple types of positive ions and negative ions, and extra transport equations to account for the transport of the turbulence kinetic energy and its specific dissipation rate.

Some test cases relevant to plasma aerodynamics were presented in which an air plasma interacts with a compressible supersonic turbulent boundary layer. The test cases were set up so that the thickness of the nonneutral sheath near the cathode was approximately the same as the one of the turbulent boundary layer, which resulted in a significant dependence of the boundary layer on the charged species and vice versa. It was then demonstrated that the proposed coupled drift-diffusion and Navier–Stokes system can be converged to the steady state in less than a couple of thousand iterations, which is commensurate with the number of iterations needed to solve the standalone Navier–Stokes equations with no plasma or chemistry effects. Such corresponds to a hundredfold or more reduction in the number of iterations to reach convergence compared to previous attempts at solving plasma flow control using the drift-diffusion model.

The proposed coupled system of equations provides yet another computational advantage by limiting errors associated with solving a set of equations with two different integration strategies. Indeed, the current approach integrates all transport equations (either related to the charged species or the neutrals) using one integration strategy that is in contrast to previous loosely coupled simulations of plasma flow control in which the charged species transport equations were solved using an integration process separate from the one used to integrate the neutrals transport equations. Using two integration processes for transport equations that depend on each other can be particularly difficult to accomplish at the discrete level and lead to errors in the preservation of monotonicity or the conservation of the fluxes. Such issues are avoided here because all transport equations are solved conjunctly.

Because the proposed coupling between the drift-diffusion and the Navier–Stokes equations offers major computational advantages with no associated drawback, it is highly recommended as a substitute to the loosely coupled approach of solving the neutrals and the charged species transport equations using two integration strategies. Such not only avoids a cumbersome dual-integration process leading to possible monotonicity or conservation errors but yields an estimated 100-fold reduction in computational effort.

Appendix: Charged Species Joule Heating

The Joule heating due to the presence of electrons and ions in a plasma corresponds to the difference between the work done on the charged species in the lab reference frame and the work done by the charged species on the neutrals also in the lab reference frame,

$$Q_J = \underbrace{\sum_{r=1}^{n_{cs}} (C_r N_r (\boldsymbol{E} + \boldsymbol{V}^r \times \boldsymbol{B}) - \nabla P_r) \cdot \boldsymbol{V}^r}_{\text{work done on the charged species in the lab frame}} - \underbrace{\left(\rho_c \boldsymbol{E} + \boldsymbol{J} \times \boldsymbol{B} - \sum_{r=1}^{n_{cs}} \nabla P_r \right) \cdot \boldsymbol{V}^n}_{\text{work done by the charged species on the neutrals in the lab frame}} \tag{A1}$$

where n_{cs} is the number of charged species. After substituting the current density $\boldsymbol{J} \equiv \sum_{r=1}^{n_{cs}} C_r N_r \boldsymbol{V}^r$ and the net charge density $\rho_c \equiv \sum_{r=1}^{n_{cs}} C_r N_r$ and simplifying, we obtain

$$Q_J = \sum_{r=1}^{n_{cs}} (C_r N_r \boldsymbol{E} + C_r N_r \boldsymbol{V}^r \times \boldsymbol{B} - \nabla P_r) \cdot (\boldsymbol{V}^r - \boldsymbol{V}^n) \tag{A2}$$

Then, from the drift-diffusion momentum equation used herein, the first term on the right-hand side can be expressed as (see Eq. (2) in Ref. [36])

$$C_r N_r (\boldsymbol{E} + \boldsymbol{V}^r \times \boldsymbol{B}) - \nabla P_r = \frac{|C_r| N_r}{\mu_r} (\boldsymbol{V}^r - \boldsymbol{V}^n) \tag{A3}$$

Substitute the latter in the former, and reformat:

$$Q_J = \sum_{r=1}^{n_{cs}} \frac{|C_r| N_r}{\mu_r} (\boldsymbol{V}^r - \boldsymbol{V}^n) \cdot (\boldsymbol{V}^r - \boldsymbol{V}^n) \tag{A4}$$

From the latter, it is obvious that the Joule heating associated with the rth charged species corresponds to

$$Q_J^r = \frac{|C_r| N_r}{\mu_r} |\boldsymbol{V}^r - \boldsymbol{V}^n|^2 \tag{A5}$$

while the total Joule heating corresponds to the sum of the Joule heating of each charged species:

$$Q_J = \sum_{r=1}^{n_{cs}} Q_J^r \tag{A6}$$

References

[1] Patel, M., Ng, T., Vasudevan, S., Corke, T., and He, S., "Aerodynamic Control Using Windward-Surface Plasma Actuators on a Separation Ramp," *Journal of Aircraft*, Vol. 44, No. 6, 2007, pp. 1889–1895. doi:10.2514/1.30741

[2] Greenblatt, D., Kastantin, Y., Nayeri, C. N., and Paschereit, C. O., "Delta-Wing Flow Control Using Dielectric Barrier Discharge Actuators," *AIAA Journal*, Vol. 46, No. 6, 2008, pp. 1554–1560. doi:10.2514/1.33808

[3] Li, Y.-H., Wu, Y., Zhou, M., Su, C.-B., Zhang, X.-W., and Zhu, J.-Q., "Control of the Corner Separation in a Compressor Cascade by Steady and Unsteady Plasma Aerodynamic Actuation," *Experiments in Fluids*, Vol. 48, No. 6, 2010, pp. 1015–1023. doi:10.1007/s00348-009-0787-2

[4] Thomas, F., Kozlov, A., and Corke, T., "Plasma Actuators for Cylinder Flow Control and Noise Reduction," *AIAA Journal*, Vol. 46, No. 8, 2008, pp. 1921–1931. doi:10.2514/1.27821

[5] Huang, X., and Zhang, X., "Streamwise and Spanwise Plasma Actuators for Flow-Induced Cavity Noise Control," *Physics of Fluids*, Vol. 20, No. 3, 2008, Paper 037101. doi:10.1063/1.2890448

[6] Grundmann, S., and Tropea, C., "Experimental Transition Delay Using Glow-Discharge Plasma Actuators," *Experiments in Fluids*, Vol. 42, No. 4, 2007, pp. 653–657. doi:10.1007/s00348-007-0256-8

[7] Hanson, R., Lavoie, P., Naguib, A., and Morrison, J., "Transient Growth Instability Cancelation by a Plasma Actuator Array," *Experiments in Fluids*, Vol. 49, No. 6, 2010, pp. 1339–1348. doi:10.1007/s00348-010-0877-1

[8] Hanson, R., Bade, K., Belson, B., Lavoie, P., Naguib, A., and Rowley, C., "Feedback Control of Slowly-Varying Transient Growth by an Array of Plasma Actuators," *Physics of Fluids*, Vol. 26, No. 2, 2014, Paper 024102. doi:10.1063/1.4863178

[9] Im, S., Do, H., and Cappelli, M. A., "Dielectric Barrier Discharge Control of a Turbulent Boundary Layer in a Supersonic Flow," *Applied Physics Letters*, Vol. 97, No. 4, 2010, Paper 041503. doi:10.1063/1.3473820

[10] Benard, N., Bonnet, J. P., Touchard, G., and Moreau, E., "Flow Control by Dielectric Barrier Discharge Actuators: Jet Mixing Enhancement," *AIAA Journal*, Vol. 46, No. 9, 2008, pp. 2305–2293. doi:10.2514/1.35404

[11] Kalra, C. S., Zaidi, S. H., Miles, R. B., and Macheret, S. O., "Shockwave-Turbulent Boundary Layer Interaction Control Using Magnetically Driven Surface Discharges," *Experiments in Fluids*, Vol. 50, No. 3, 2011, pp. 547–559. doi:10.1007/s00348-010-0898-9

[12] Lineberry, J. T., Begg, L., Castro, J. H., Litchford, R. J., and Donohue, J., "HVEPS Scramjet-Driven MHD Power Demonstration Test Results," *38th AIAA Plasmadynamics and Lasers Conference*, AIAA Paper 2007-3880, 2007.

[13] Surzhikov, S. T., and Shang, J. S., "Two-Component Plasma Model for Two-Dimensional Glow Discharge in Magnetic Field," *Journal of Computational Physics*, Vol. 199, No. 2, 2004, pp. 437–464. doi:10.1016/j.jcp.2004.02.019

[14] Likhanskii, A. V., Shneider, M. N., Macheret, S. O., and Miles, R. B., "Modeling of Dielectric Barrier Discharge Plasma Actuators Driven by Repetitive Nanosecond Pulses," *Physics of Plasmas*, Vol. 14, No. 7, 2007, Paper 073501. doi:10.1063/1.2744227

[15] Poggie, J., "Numerical Simulation of Direct Current Glow Discharges for High-Speed Flow Control," *Journal of Propulsion and Power*, Vol. 24, No. 5, 2008, pp. 916–922. doi:10.2514/1.24403

[16] Shang, J. S., and Huang, P. G., "Modeling of AC Dielectric Barrier Discharge," *Journal of Applied Physics*, Vol. 107, No. 11, 2010, Paper 113302. doi:10.1063/1.3415526

[17] Shang, J. S., Roveda, F., and Huang, P. G., "Electrodynamic Force of Dielectric Barrier Discharge," *Journal of Applied Physics*, Vol. 109, No. 11, 2011, Paper 113301. doi:10.1063/1.3585853

[18] Hoskinson, A. R., and Hershkowitz, N., "Modelling of Dielectric Barrier Discharge Plasma Actuators with Thick Electrodes," *Journal of Physics D: Applied Physics*, Vol. 44, No. 8, 2011. doi:10.1088/0022-3727/44/8/085202

[19] Surzhikov, S., *Computational Physics of Electric Discharges in Gas Flows*, De Gruyter, Berlin, 2012.

[20] Poggie, J., Adamovich, I., Bisek, N., and Nishihara, M., "Numerical Simulation of Nanosecond-Pulse Electrical Discharges," *Plasma Sources Science and Technology*, Vol. 22, No. 1, 2013, Paper 015001. doi:10.1088/0963-0252/22/1/015001

[21] Shyy, W., Jayaraman, B., and Andersson, A., "Modeling of Glow Discharge-Induced Fluid Dynamics," *Journal of Applied Physics*, Vol. 92, No. 11, 2002, pp. 6434–6443. doi:10.1063/1.1515103

[22] Singh, K., and Roy, S., "Force Approximation for a Plasma Actuator Operating in Atmospheric Air," *Journal of Applied Physics*, Vol. 103, No. 1, 2008, Paper 013305. doi:10.1063/1.2827484

[23] Rizzetta, D. P., and Visbal, M. R., "Large Eddy Simulation of Plasma Based Control Strategies for Bluff Body Flow," *AIAA Journal*, Vol. 47, No. 3, 2009, pp. 717–729. doi:10.2514/1.39168

[24] Atkinson, M. D., Poggie, J., and Camberos, J. A., "Control of Separated Flow in a Reflected Shock Interaction Using a Magnetically-Accelerated Surface Discharge," *Physics of Fluids*, Vol. 24, No. 12, 2012, Paper 126102. doi:10.1063/1.4772197

[25] Rizzetta, D., and Visbal, M., "Plasma Flow Control Simulations of a Low-Reynolds Number Low-Aspect-Ratio Wing," *Computers and Fluids*, Vol. 70, 2012, pp. 95–114. doi:10.1016/j.compfluid.2012.08.025

[26] Bisek, N. J., Rizzetta, D. P., and Poggie, J., "Plasma Control of a Turbulent Shock Boundary-Layer Interaction," *AIAA Journal*, Vol. 51, No. 8, 2013, pp. 1789–1804. doi:10.2514/1.J052248

[27] Duchmann, A., Simon, B., Tropea, C., and Grundmann, S., "Dielectric Barrier Discharge Plasma Actuators for In-Flight Transition Delay," *AIAA Journal*, Vol. 52, No. 2, 2014, pp. 358–367. doi:10.2514/1.J052485

[28] Poggie, J., and Gaitonde, D. V., "Magnetic Control of Flow Past a Blunt Body: Numerical Validation and Exploration," *Physics of Fluids*,

Vol. 14, No. 5, 2002, pp. 1720–1731.
doi:10.1063/1.1465424
[29] Parent, B., Macheret, S., Shneider, M., and Harada, N., "Numerical Study of an Electron-Beam-Confined Faraday Accelerator," *Journal of Propulsion and Power*, Vol. 23, No. 5, 2007, pp. 1023–1032.
doi:10.2514/1.26936
[30] Wan, T., Candler, G. V., Macheret, S. O., and Shneider, M. N., "Three-Dimensional Simulation of the Electric Field and Magnetohydrodynamic Power Generation During Reentry," *AIAA Journal*, Vol. 47, No. 6, 2009, pp. 1327–1336.
doi:10.2514/1.32006
[31] Surzhikov, S. T., "Glow Discharge in External Magnetic Field in Hypersonic Flow of Rarefied Gas," *High Temperature*, Vol. 47, No. 4, 2009, pp. 459–471.
doi:10.1134/S0018151X09040026
[32] Bityurin, V. A., Bocharov, A. N., and Popov, N. A., "Numerical Simulation of an Electric Discharge in Supersonic Flow," *Fluid Dynamics*, Vol. 43, No. 4, 2008, pp. 642–653.
doi:10.1134/S0015462808040170
[33] Parent, B., Shneider, M. N., and Macheret, S. O., "Sheath Governing Equations in Computational Weakly-Ionized Plasmadynamics," *Journal of Computational Physics*, Vol. 232, No. 1, 2013, pp. 234–251.
doi:10.1016/j.jcp.2012.08.011
[34] Parent, B., Macheret, S. O., and Shneider, M. N., "Ambipolar Diffusion and Drift in Computational Weakly-Ionized Plasmadynamics," *Journal of Computational Physics*, Vol. 230, No. 22, 2011, pp. 8010–8027.
doi:10.1016/j.jcp.2011.07.006
[35] Parent, B., Macheret, S. O., and Shneider, M. N., "Electron and Ion Transport Equations in Computational Weakly-Ionized Plasmadynamics," *Journal of Computational Physics*, Vol. 259, Feb. 2014, pp. 51–69.
doi:10.1016/j.jcp.2013.11.029
[36] Parent, B., Macheret, S. O., and Shneider, M. N., "Modeling Weakly-Ionized Plasmas in Magnetic Field: A New Computationally-Efficient Approach," *Journal of Computational Physics*, Vol. 300, Nov. 2015, pp. 779–799.
doi:10.1016/j.jcp.2015.08.010
[37] Parent, B., Shneider, M. N., and Macheret, S. O., "Generalized Ohm's Law and Potential Equation in Computational Weakly-Ionized Plasmadynamics," *Journal of Computational Physics*, Vol. 230, No. 4, 2011, pp. 1439–1453.
doi:10.1016/j.jcp.2010.11.012
[38] Wilcox, D. C., "Reassessment of the Scale Determining Equation for Advanced Turbulence Models," *AIAA Journal*, Vol. 26, No. 11, 1988, pp. 1299–1310.
doi:10.2514/3.10041
[39] Aleksandrov, N. L., Bazelyan, E. M., Kochetov, I. V., and Dyatko, N. A., "The Ionization Kinetics and Electric Field in the Leader Channel in Long Air Gaps," *Journal of Physics D: Applied Physics*, Vol. 30, No. 11, 1997, pp. 1616–1624.
doi:10.1088/0022-3727/30/11/011
[40] Kossyi, A., Kostinsky, A. Y., Matveyev, A. A., and Silakov, V. P., "Kinetic Scheme of the Non-Equilibrium Discharge in Nitrogen-Oxygen Mixtures," *Plasma Sources Science and Technology*, Vol. 1, No. 3, 1992, pp. 207–220.
doi:10.1088/0963-0252/1/3/011
[41] Bazelyan, E. M., and Raizer, Y. P., *Spark Discharge*, CRC Press, Boca Raton, FL, 1997.
[42] Bychkov, Y. I., Korolev, Y. D., and Mesyats, G. A., *Inzhektsionnaia Gazovaia Elektronika*, Nauka, Novosibirsk, Russia, 1982 (in Russian).
[43] Krivonosova, O. E., Losev, S. A., Nalivayko, V. P., Mukoseev, Y. K., and Shatalov, O. P., *Khimiia Plazmy*, edited by Smirnov, B. M., Vol. 14, Energoatomizdat, Moscow, 1987, p. 3.
[44] McBride, B. J., Zehe, M. J., and Gordon, S., "NASA Glenn Coefficients for Calculating Thermodynamic Properties of Individual Species," NASA TP-211556, Sept. 2002.
[45] Aleksandrov, N. L., Vysikailo, F. I., Islamov, R. S., Kochetov, I. V., Napartovich, A. P., and Pevgov, V. G., "Electron Distribution Function in 4:1 N2-O2 Mixture," *High Temperature*, Vol. 19, No. 1, 1981, pp. 17–21.
[46] Grigoriev, I. S., and Meilikhov, E. Z., *Handbook of Physical Quantities*, CRC Press, Boca Raton, FL, 1997.
[47] Anderson, J. D., *Hypersonic and High-Temperature Gas Dynamics*, McGraw–Hill, New York, 1989.
[48] Barrow, G. M., *Introduction to Molecular Spectroscopy*, McGraw–Hill Education, New York, 1962.
[49] Macheret, S. O., Shneider, M. N., and Miles, R. B., "Electron-Beam-Generated Plasmas in Hypersonic Magnetohydrodynamic Channels," *AIAA Journal*, Vol. 39, No. 6, 2001, pp. 1127–1138.
doi:10.2514/2.1426
[50] Wilcox, D. C., *Turbulence Modeling for CFD*, 2nd ed., DCW Industries, La Cañada, CA, 1998.
[51] Dixon-Lewis, G., "Computer Modelling of Combustor Reactions," *Combustion Chemistry*, edited by Gardiner, W. C., Springer–Verlag, New York, 1984.
[52] Gershenzon, Y. M., Rozenshtein, V., and Umansky, S., "Heterogeneous Relaxation of Vibrational Energy of Molecules," *Khimiia Plazmy*, edited by Smirnov, B. M., Vol. 4, Energoatomizdat, Moscow, 1977, pp. 61–97 (in Russian).
[53] Black, G., Wise, H., Schechter, S., and Sharpless, R., "Measurements of Vibrationally Excited Molecules by Raman Scattering," *Journal of Chemical Physics*, Vol. 60, No. 9, 1974, p. 3526–3536.
doi:10.1063/1.1681570
[54] Raizer, Y. P., and Shneider, M. N., "Electrodeless Capacitive Discharge Sustained by Repetitive High-Voltage Pulses," *High Temperature*, Vol. 27, No. 3, 1989, pp. 329–335 (in English).
[55] Roe, P. L., "Approximate Riemann Solvers, Parameter Vectors, and Difference Schemes," *Journal of Computational Physics*, Vol. 43, No. 2, 1981, pp. 357–372.
doi:10.1016/0021-9991(81)90128-5
[56] Yee, H. C., Klopfer, G. H., and Montagné, J.-L., "High-Resolution Shock-Capturing Schemes for Inviscid and Viscous Hypersonic Flows," *Journal of Computational Physics*, Vol. 88, No. 1, 1990, pp. 31–61.
doi:10.1016/0021-9991(90)90241-R
[57] Parent, B., "Positivity-Preserving High-Resolution Schemes for Systems of Conservation Laws," *Journal of Computational Physics*, Vol. 231, No. 1, 2012, pp. 173–189.
doi:10.1016/j.jcp.2011.09.006
[58] Viviand, H., "Conservative Forms of Gas Dynamics Equations," *La Recherche Aérospatiale*, No. 1, Jan. 1974, pp. 65–68.
[59] Vinokur, M., "Conservative Equations of Gas-Dynamics in Curvilinear Coordinate Systems," *Journal of Computational Physics*, Vol. 14, No. 2, 1974, pp. 105–125.
doi:10.1016/0021-9991(74)90008-4
[60] Peaceman, D. W., and Rachford, H. H., "The Numerical Solution of Parabolic and Elliptic Differential Equations," *Journal of the Society for Industrial and Applied Mathematics*, Vol. 3, No. 1, 1955, pp. 28–41.
doi:10.1137/0103003
[61] Douglas, J., Jr., "On the Numerical Integration of by Implicit Methods," *Journal of the Society for Industrial and Applied Mathematics*, Vol. 3, No. 1, 1955, pp. 42–65.
doi:10.1137/0103004
[62] Briley, W. R., and McDonald, H., "On the Structure and Use of Linearized Block Implicit Schemes," *Journal of Computational Physics*, Vol. 34, No. 1, 1980, pp. 54–73.
doi:10.1016/0021-9991(80)90112-6
[63] Oran, E., and Boris, J. P., *Numerical Simulation of Reactive Flow*, 2nd ed., Cambridge Univ. Press, New York, 2001.
[64] Parent, B., and Sislian, J. P., "Validation of the Wilcox Model for Flows Characteristic to Hypersonic Airbreathing Propulsion," *AIAA Journal*, Vol. 42, No. 2, 2004, pp. 261–270.
doi:10.2514/1.1989
[65] Parent, B., "Positivity-Preserving Flux Difference Splitting Schemes," *Journal of Computational Physics*, Vol. 243, No. 1, 2013, pp. 194–209.
doi:10.1016/j.jcp.2013.02.048
[66] Raizer, Y. P., *Gas Discharge Physics*, Springer–Verlag, Berlin, 1991.

Y. Ju
Associate Editor